https://doi.org/10.5194/egusphere-2023-1320
Preprint. Discussion started: 28 July 2023

Extreme melting at Greenland's largest floating ice tongue

Ole Zeising[1,2], Niklas Neckel[1], Nils Dörr[3,4], Veit Helm[1], Daniel Steinhage[1], Ralph Timmermann[1], and Angelika Humbert[1,2]

[1]Alfred-Wegener-Institut Helmholtz-Zentrum für Polar- und Meeresforschung, Bremerhaven, Germany
[2]Department of Geosciences, University of Bremen, Bremen, Germany
[3]Institute of Geosciences, Kiel University, Kiel, Germany
[4]Institute of Photogrammetry and Remote Sensing, Karlsruhe Institute of Technology (KIT), Karlsruhe, Germany

Correspondence: Ole Zeising (ole.zeising@awi.de)

Abstract. The 79° North Glacier (Nioghalvfjerdsbrae, 79NG) is one of three remaining glaciers with a floating tongue in Greenland. Although the glacier was considered exceptionally stable in the past, earlier studies indicate that the ice tongue has thinned in recent decades. By conducting high-resolution ground-based and airborne radar measurements in conjunction with satellite remote sensing observations, we find significant changes in the geometry of 79NG. In the vicinity of the grounding line, a $500\,\mathrm{m}$ high subglacial channel has grown since ~2010 and caused surface lowering of up to $7.6\,\mathrm{m\,a^{-1}}$. Our results show extreme basal melt rates exceeding $150\,\mathrm{m\,a^{-1}}$ within a distance of $5\,\mathrm{km}$ from the grounding line, where the ice has thinned by 42% since 1998. We found a heterogeneous distribution of melt rates likely due to variability in water column thickness and channelization of the ice base. Time series of melt rates show a decrease in basal melting since 2018, indicating an inflow of colder water into the cavity below 79NG. We discuss the processes that have led to the changes in geometry and conclude that the inflow of warm ocean currents has led to the extensive thinning of 79NG's floating ice tongue near the grounding line in the last two decades. In contrast, we hypothesize that the growth of the channel results from increased subglacial discharge due to a considerably enlarged area of summer surface melt due to the warming of the atmosphere.

1 Introduction

The mass loss of the Greenland Ice Sheet over the last decades as a result of a warming atmosphere and ocean has accelerated (Shepherd et al., 2020) and contributed to recent sea-level rise by $1.4\,\mathrm{mm\,a^{-1}}$ (Khan et al., 2022a). Half of the mass loss is caused by ice-sheet discharge through marine-terminating glaciers (Shepherd et al., 2020), mainly due to the retreat of glacier fronts (King et al., 2020) as the floating ice tongues restrain the outflow of the grounded ice (Fürst et al., 2016). The largest of the three remaining floating tongues in Greenland is the one of Nioghalvfjerdsbrae (79NG). Together with its neighboring Zachariæ Isstrøm (ZI), it is the main outlet glacier of the Northeast Greenland Ice Stream (NEGIS; Fig. 1a), the largest ice stream of the Greenland Ice Sheet (Fahnestock et al., 2001). After the collapse of ZI's floating tongue in 2002, the glacier itself (Khan et al., 2014; Mouginot et al., 2015), as well as NEGIS, have shown an extensive speed-up (Khan et al., 2022b). In contrast, only minor acceleration rates have been observed at 79NG (Mouginot et al., 2015; Vijay et al., 2019).

https://doi.org/10.5194/egusphere-2023-1320
Preprint. Discussion started: 28 July 2023

Ice sheet simulations indicate that 79NG remains stable within this century and will experience only a minor grounding line retreat as bedrock rises inland (Choi et al., 2017). Its stability is attributed to pinning points at the calving front (Thomsen et al., 1997), lateral resistance from shear margins (Mayer et al., 2000; Rathmann et al., 2017; Mayer et al., 2018) and confinement of the glacier leading to lateral compression. However, thinning has occurred during the last two decades (Helm et al., 2014; Kjeldsen et al., 2015; Mouginot et al., 2015; Mayer et al., 2018) and cracks have formed at the calving front that might be a precursor of disintegration (Humbert et al., 2022b).

Observations and modeling show that the inflow of warm Atlantic Intermediate Water (AIW, temperatures exceeding 1 °C) into the cavity below 79NG (Straneo et al., 2012; Wilson and Straneo, 2015; Lindeman et al., 2020; Schaffer et al., 2020) and its variability are connected to the ocean currents in Fram Strait (Münchow et al., 2020; von Albedyll et al., 2021). Bentley et al. (2023) gives evidence that the AIW reaches the grounding line area of 79NG a few months after the inflow into the cavity.

The observed oceanic heat transport into the sub-ice cavity (Schaffer et al., 2020) has been suggested to maintain intense basal melting (Mayer et al., 2018; Lindeman et al., 2020; Schaffer et al., 2020). Similar processes might have led to the disintegration and retreat of the floating ice tongues of Jakobshavn Isbræ (Motyka et al., 2011). However, the supply of fresh water from glacier surface melting was found to alter circulation in fjords and basal melting of glaciers (Straneo et al., 2016). In the future, submarine melt rates are expected to increase most pronouncedly in the northeastern part of Greenland towards the end of the 21st century (Slater et al., 2020).

Observations of basal melt rates and their influence on the ice thickness are thus considered key to understanding the dynamics of the system. Basal melt rates of 79NG have been estimated based on indirect satellite remote sensing retrievals (Wilson et al., 2017), which are accompanied by considerable uncertainties and limited to freely floating parts. Especially in the area of the grounding line of 79NG where higher basal melt rates are expected due to thick (reduced melting temperature) ice getting into contact with warm ocean waters, other methods must be used to monitor changes in ice thickness and to understand the underlying processes.

In this study, we investigate the recent changes in ice thickness of the 79NG from in-situ and airborne as well as satellite remote sensing observations. We analyze a spatial distribution of thinning and basal melt rates focusing on the vicinity of the grounding line of 79NG. Finally, we discuss the processes that explain the observations and how these have changed in the past decades.

2 Data

In order to obtain a time series of surface elevations of the 79NG grounding line area we generated 96 Digital Elevation Models (DEMs), which span the period December 2010 to April 2021. Additionally, we acquired airborne and ground-based radar measurements at the 79NG under the framework of the *Greenland Ice Sheet – Ocean Interaction* (GROCE) project. The airborne radar measurements were performed in April 2018 and July 2021 with the ultra-wideband (UWB) radar in order to determine the basal geometry of the 79NG. We obtained a spatial distribution of Lagrangian thinning rates from a repeat survey of ground-based phase-sensitive radar (pRES) measurements in July 2017 and 2018. In July 2017, we marked the measurement

https://doi.org/10.5194/egusphere-2023-1320
Preprint. Discussion started: 28 July 2023

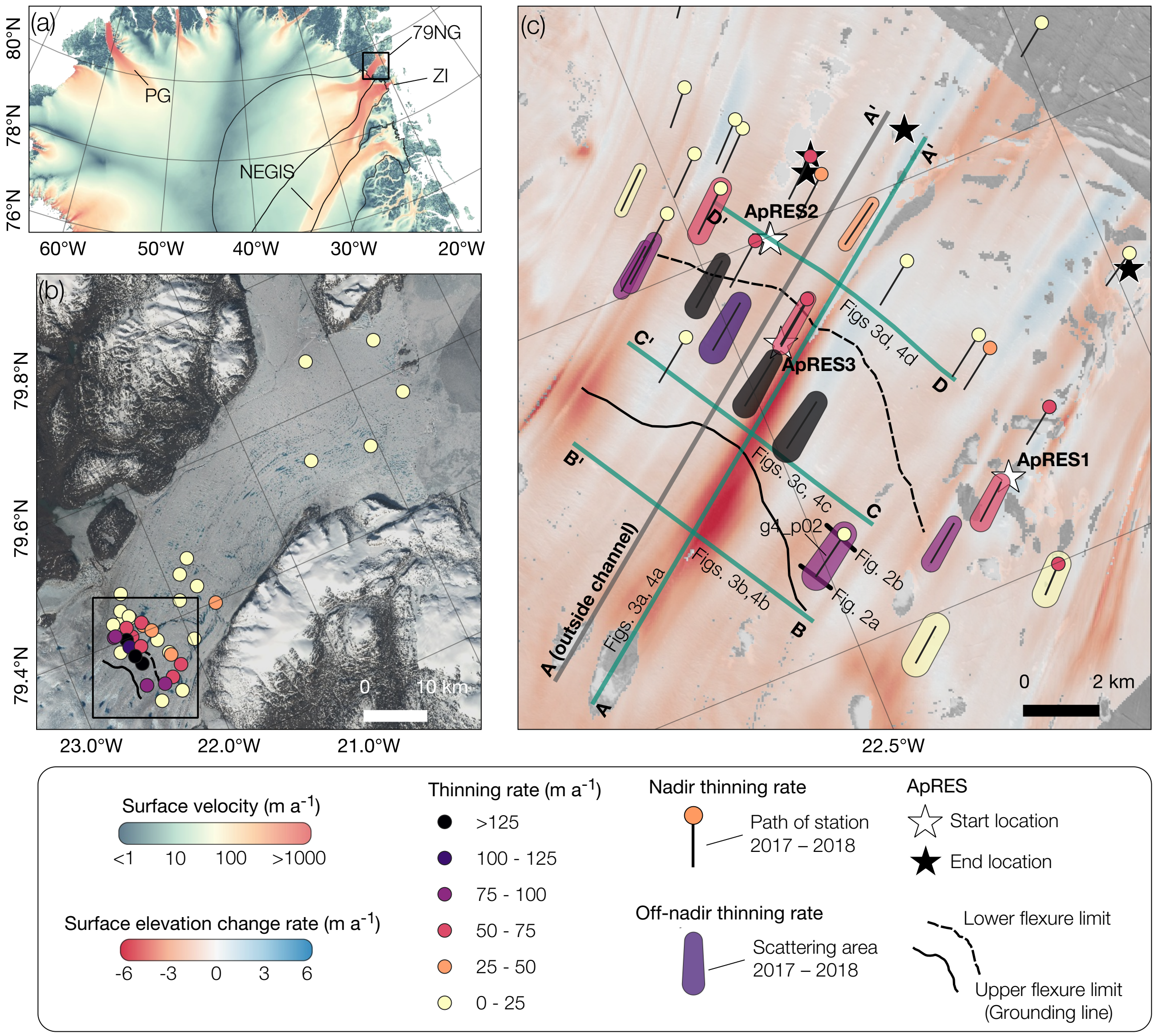

Figure 1. (a) Map of northern Greenland with drainage basins (black lines) of 79NG and Zachariæ Isstrøm (ZI) (Krieger et al., 2020) and surface velocities (Joughin et al., 2018) showing the Northeast Greenland Ice Stream (NEGIS) and Petermann Glacier (PG). (b) Sentinel-2 mosaic of 79NG with thinning rates derived from in-situ measurements in 2017 and 2018 (box in (a)). (c) Enlargement of the 79NG hinge zone (box in (b)) with surface elevation change rates (dh/dt) derived from TanDEM-X satellite data between 2010 and 2021. Dots and squares showing nadir and off-nadir thinning rates with paths of Lagrangian measurement location between July 2017 and July 2018. White stars mark the starting and black stars the ending position of ApRES stations. Copernicus Sentinel data from 2018, retrieved from Copernicus SciHub on 16 August 2021.

https://doi.org/10.5194/egusphere-2023-1320
Preprint. Discussion started: 28 July 2023

location on the surface by $4\,\mathrm{m}$ long bamboo stakes drilled into the ice in order to be able to repeat the measurement in 2018 at exactly the same location in the Lagrangian frame. The majority of the measurement locations were distributed within $8\,\mathrm{km}$ distance from the grounding line (Fig. 1b). Here, we operated autonomous pRES stations at three locations (ApRES1-3) until June 2022 that move with the ice to derive year-round time series of basal melt rates in a Lagrangian reference frame. In Summer 2018, we relocated ApRES2 to its starting position from 2016 in order to repeat the measurements on the same flowline. These stations are labeled as ApRES2a (2016–2018) and ApRES2b (2018–2019).

3 Methods

3.1 Time series of surface elevations from TanDEM-X SAR interferometry

DEMs were generated from bistatic TanDEM-X SAR interferometry closely following the methods described by Neckel et al. (2013). Interferograms were formed from co-registered Single-look Slant range Complex (CoSSC) data employing a $4{\times}4$ multi-looking step. Prior to phase unwrapping we subtracted a simulated phase from the global TanDEM-X DEM at 30 m resolution (Wessel et al., 2016). The latter was done to reduce unwrapping errors and the simulated phase was added back afterwards. The final DEMs were geocoded and spatially adjusted to the global TanDEM-X DEM over stable bedrock following the methods described by Nuth and Kääb (2011). Surface elevation changes between 2010 and 2021 were estimated by fitting a linear trend to every pixel of the co-registered stack of 96 DEMs (e.g. Berthier et al., 2016).

3.2 Ultra-wideband (UWB) airborne radar

The UWB is a multichannel coherent airborne radar that consists of an eight-element antenna array with a total transmit power of $6\,\mathrm{kW}$ (Hale et al., 2016). The antennas operate in the frequency band of 150 – $520\,\mathrm{MHz}$, with a pulse repetition frequency of $10\,\mathrm{kHz}$ and a sampling frequency of $1.6\,\mathrm{GHz}$. The characteristics of the transmitted waveform and the recording settings can be manually adjusted. We used alternating sequences of different transmission/recording settings (waveforms) to increase the dynamic range: short pulses ($1\,\mu\mathrm{s}$) and low receiver gain (11 – $13\,\mathrm{dB}$) to image the glacier surface, and longer pulses (3 – $10\,\mu\mathrm{s}$) with higher receiver gain ($48\,\mathrm{dB}$) to image internal features and the ice base. The waveforms were defined with regard to the glacier thickness. Additionally, we used two different frequency bands in the survey: 180 – $210\,\mathrm{MHz}$ and 150 – $520\,\mathrm{MHz}$. The theoretical range resolution in ice after pulse-compression for the two bandwidths is about $2.8\,\mathrm{m}$ and $0.23\,\mathrm{m}$, respectively. Recorded traces were presumed in the hardware by a factor between 2 and 16, depending on the pulse length. In order to reduce range side lobes, the transmitted and the received signals were tapered using a Tukey window and the received signal spectrum was filtered with a Hanning window (The MathWorks Inc., 2022). We recorded the position of the aircraft with four NovAtel GPS receivers, which were mounted on the wings and the fuselage.

Post-flight processing included pulse compression in the range direction, synthetic aperture radar focusing in the along-track direction, and array processing in the cross-track direction to suppress off-nadir echoes. To transform two-way travel time to depth, we used a propagation velocity for the electromagnetic wave of $168.914\,\mathrm{m}\,\mu\mathrm{s}^{-1}$ that refers to a relative permittivity

https://doi.org/10.5194/egusphere-2023-1320
Preprint. Discussion started: 28 July 2023

of $\varepsilon_r = 3.15$ for pure ice. No firn correction was applied since the predominant part of the glacier is located in the ablation zone. We concatenated the echograms of the alternating waveforms to obtain the final echograms covering the glacier from the surface to the base with a high dynamic range. Finally, the surface return of the radar echo was aligned with a high-resolution elevation model created from simultaneously acquired laser scanner data.

3.3 Phase-sensitive Radio Echo Sounder (pRES)

3.3.1 Technical Background

The phase-sensitive radio echo sounder (pRES) is a ground-penetrating frequency-modulated continuous-wave (FMCW) radar, transmitting chirps with a frequency bandwidth of $200\,\mathrm{MHz}$ and a center frequency of $300\,\mathrm{MHz}$ (Brennan et al., 2014; Nicholls et al., 2015). The same device can be operated in an autonomous mode (henceforth *ApRES*) to perform measurements over a longer period of time with a defined interval. While the repeat pRES survey was performed with 100 chirps and two skeleton slot antennas, the ApRES stations consist of two bow-tie antennas and recorded 20 chirps with a measuring interval between one and six hours. For processing the raw data, we calculated pairwise correlation coefficients of all chirps, rejected chirps with low correlation coefficients, and stacked the remaining ones. We followed Brennan et al. (2014) for processing to get amplitude- and phase-depth profiles. We assumed a relative permittivity of $\varepsilon_r = 3.15$ in ice for the time-to-depth conversion.

3.3.2 Thinning rates from single-repeated pRES measurements

The estimation of the Lagrangian thinning rate is based on the change in ice thickness along the flow of the same ice particles. The ice base is assumed to be responsible for strong peaks in the radar signal due to the high contrast in relative permittivity between ice and seawater. In the case of a flat ice base, the nadir reflection has the shortest two-way travel time of all basal reflections in a radius defined by the antenna beamwidth. However, steep basal gradients such as those of basal channels can cause off-nadir reflections which might appear before the nadir basal return. In order to identify nadir and off-nadir returns, we used the ice base – ice surface – ice base multiple which we assume to be the strongest for the nadir reflections. The reflected energy from a far-off-nadir reflection will be mostly reflected in the opposite direction in the case of a flat ice surface. Therefore, multiples from off-nadir reflections will be weaker compared to nadir reflections. Additionally, we used the ice thickness distribution derived from UWB echograms nearby the location of the pRES observations that can reveal the ice thickness and, furthermore, give a hint for the origin of the recorded off-nadir reflection. At pRES location g4_p02, UWB echograms from 2018 show a growing subglacial channel in the immediate vicinity of both the first and repeated pRES measurement (Figs. 1c, 2). Based on these UWB echograms, we link the origin of the off-nadir reflection to the basal channel. In Appendix A, we give further examples of amplitude profiles from repeated pRES measurements where the first basal return was identified to be an off-nadir return. The distinction between nadir and off-nadir returns is important as the precise local change in ice thickness can only be revealed from nadir returns. Following Stewart et al. (2019), we applied a cross-correlation of the amplitude and the phase of their basal segments ranging from -9 to $+1\,\mathrm{m}$ around the identified return. The uncertainty in this case is below $0.01\,\mathrm{m}$.

https://doi.org/10.5194/egusphere-2023-1320
Preprint. Discussion started: 28 July 2023

Even if no distinction between nadir and off-nadir reflection can be made, the ice thickness change can be estimated with the following approach: Using the first basal return in both measurements would always result in an underestimation of the change in ice thickness at least at one of both locations where the (off-nadir) first basal reflections occurred (Appendix A). This means that a thinning rate exists somewhere in the scattering area that is as large as this amount or even more. Note, this should not be understood as the minimum rate in the scattered area (marked in Fig. 1 for off-nadir thinning rates), as there can also be lower thinning rates at the same time. Thus, at stations where we could not distinguish reliably between a nadir and an off-nadir reflection, we used the first strong increase in amplitude for the ice thickness calculation and interpret this as an off-nadir return. The range to the off-nadir basal reflector differs from the ice thickness above the reflector, which can be derived by $H^\alpha = R\cos\alpha$, where R is the range of the basal reflector and H^α the off-nadir ice thickness viewed at an angle α. The resulting thinning rate $\Delta\dot{H}^\alpha$ (positive values correspond to thinning) is

$$\Delta\dot{H}^\alpha = -\frac{(R_2 - R_1)\cos\alpha}{\Delta t}, \tag{1}$$

where R_1 is the range to the off-nadir basal reflector of the first and R_2 of the second measurement after the time period Δt. Since the off-nadir angle α is often unknown, we assume that it ranges from 0° to a maximum of 30° (Brennan et al., 2014) and calculated the average of both angles. The spread in ice thickness difference from both α together with the inaccuracy of the signal propagation speed in the ice of $\sim 1\%$ (Fujita et al., 2000) is represented in the uncertainty of $\Delta\dot{H}^\alpha$. At those stations at which we identified nadir and off-nadir reflections, we determined both thinning rates. We rejected those measurements where the depth of the first basal return was unclear. Since the estimation of vertical strain was not possible with single-repeated pRES measurements due to the low correlation of the amplitude profiles, we could not calculate the basal melt rate.

3.3.3 Basal melt rates from ApRES time series

The calculation of basal melt rates follows previously described methods (Corr et al., 2002; Jenkins et al., 2006; Stewart et al., 2019). Several quantities cause changes to the range R to the basal reflector within the time period Δt: ablation ΔR_s, strain ΔR_ε and basal melting ΔR_b:

$$\frac{\Delta R}{\Delta t} = \frac{\Delta R_s}{\Delta t} + \frac{\Delta R_\varepsilon}{\Delta t} + \frac{\Delta R_b}{\Delta t} \tag{2}$$

With the ApRES time series (Appendix B), all of these quantities can be estimated in order to obtain the basal melt rate. Since the estimation is based on the detection of the vertical displacement of layers, we divided the first echogram in $6\,\mathrm{m}$ long segments with $5\,\mathrm{m}$ overlap starting at a depth of $20\,\mathrm{m}$. For each segment, we derived displacements from complex cross-correlation of the phase of all pairwise time-consecutive measurements (Stewart, 2018). Afterward, we calculated the daily mean values of the displacements.

In the first step, we used the time-mean vertical displacement of internal reflectors to calculate the vertical strain profile. Here only those segments between $20\,\mathrm{m}$ below the surface and $20\,\mathrm{m}$ above the basal return at the last measurement were considered. In addition, we only considered measurements between October and May to avoid the influence of ablation on the calculation

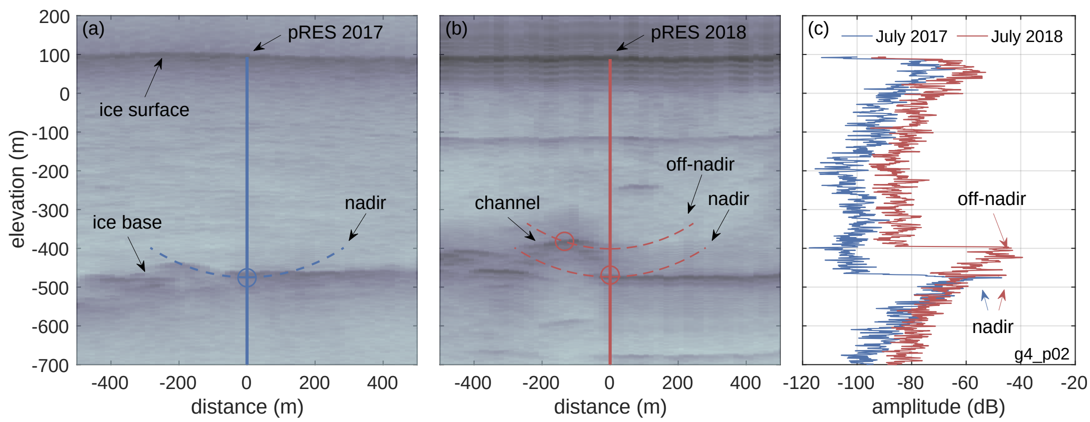

Figure 2. Growing basal channel from pRES and UWB echograms. (a,b) UWB echograms from the across-flow profiles from 2018. The center of both is the location of a Lagrangian pRES measurement in 2017 ((a), vertical blue line) and 2018 ((b), vertical red line). Possible origins of nadir and off-nadir reflections, discovered in the pRES echograms (c), are represented by dashed lines. The suggested locations at which the reflections occurred are marked by circles. (c) pRES echograms from 2017 and 2018 with the identified nadir and off-nadir reflections. Location is shown in Fig. 1c.

of the strain. The vertical strain is the depth derivative of the vertical displacement u_z

$$\varepsilon_{zz} = \frac{\partial u_z}{\partial z}, \tag{3}$$

which we derived from a linear fit that best matches the vertical displacements. Although one of the ApRES stations was located within the hinge zone in which bending might affect the strain distribution (Jenkins et al., 2006), none of the displacement distributions indicated a deviation from a linear function over depth.

For a nadir basal reflection, the estimation of the range shift due to ice deformation $\Delta R_\varepsilon^{\mathrm{n}}$ is only affected by the vertical strain

$$\Delta R_\varepsilon^{\mathrm{n}} = \int_0^R \varepsilon_{zz}\,\mathrm{d}z. \tag{4}$$

Calculating the displacement of off-nadir reflectors due to deformation is more complex because the two horizontal strain components ε_{xx} and ε_{yy} must also be considered (see Appendix B1). Since we can only determine the vertical strain component ε_{zz} with ApRES measurements, we have to make assumptions to estimate ΔR_ε viewed at an angle α. In Appendix B1, we show that for small off-nadir angles of $\alpha \leq 30°$, the absolute value of ΔR_ε is always smaller than or equal to the absolute value of the nadir displacement $\Delta R_\varepsilon^{\mathrm{n}}$:

$$0 \leq |\Delta R_\varepsilon| \leq |\Delta R_\varepsilon^{\mathrm{n}}|, \tag{5}$$

At all ApRES sites, we found $\varepsilon_{zz} > 0$ (see Appendix B2), so that Equation 5 can be simplified further to

$$0 < \Delta R_\varepsilon \leq \Delta R_\varepsilon^{\mathrm{n}}. \tag{6}$$

https://doi.org/10.5194/egusphere-2023-1320
Preprint. Discussion started: 28 July 2023

Thus, assuming that the reflection occurred from a nadir reflector, we cannot underestimate the deformation. The largest $\Delta R^{\mathrm{n}}_{\varepsilon}$ was found to be $2.7\,\mathrm{m}$ for $\Delta t = 1\,a$ at ApRES2b, which results in an underestimated melt rate of $\leq 2.7\,\mathrm{m\,a^{-1}}$ due to deformation.

Next, we use the displacement time series of the segment centered at a range of $50\,\mathrm{m}$ (u_z^{50}) to correct for ablation. Since the ice above is affected by ice deformation, we subtract this contribution from the displacement

$$\Delta R^{\mathrm{n}}_s = u_z^{50} - \int_0^{50} \varepsilon_{zz}\,\mathrm{d}z. \tag{7}$$

Here, ΔR^{n}_s is the vertical (nadir) ablation. In order to determine the contribution of the ablation to the range difference to an off-nadir reflector, ΔR^{n}_s, we need to correct for the angle α:

$$\Delta R_s = \frac{\Delta R^{\mathrm{n}}_s}{\cos\alpha}. \tag{8}$$

Since α is still unknown, we use the extremes $0°$ and $30°$ and average both values. The difference from the mean is used as uncertainty, which corresponds up to $2\,\mathrm{m\,a^{-1}}$ in summer and near zero in winter.

To finally derive the basal melt rate a_b in the vertical direction, we subtract ΔR_ε and ΔR_s from the displacement of a basal reflector

$$a_b = -\frac{\Delta R_b}{\Delta t} = -\frac{\Delta R - \Delta R_s - \Delta R_\varepsilon}{\Delta t}. \tag{9}$$

Similar to (Vaňková et al., 2021), we analyze ΔR for all segments within a range of $50\,\mathrm{m}$ below the first basal return to obtain the nadir and off-nadir basal melt rates. This range was chosen since at the ApRES sites, all strong basal reflections occurred within $50\,\mathrm{m}$. To represent the variability within a time series, we calculated the median melt rate next to the 25%, 75%, and 95% quantile for each time step. Afterward, a 7-day moving average filter was used to smooth the time series.

The largest uncertainty of the melt rate estimate arises from the unknown off-nadir angle α, which affects the ablation and strain correction. The sum of both uncertainties is up to $8\,\mathrm{m\,a^{-1}}$ in summer and significantly less in winter. In addition, the estimate of the melt rate quantifies the rate at which the ice base has approached the ApRES through melting. This can differ from the melt rate in the normal or vertical direction at the basal reflector. A further uncertainty arises from the inaccuracy of the signal propagation speed in the ice, which corresponds to $\sim 1\%$ of the melt rate (Fujita et al., 2000).

https://doi.org/10.5194/egusphere-2023-1320
Preprint. Discussion started: 28 July 2023

4 Results

4.1 Growing subglacial channel causes local surface lowering

The DEM time series reveals that the surface elevation of the 79NG has decreased along the grounding line by a rate of $-2.0 \pm 1.4\,\mathrm{m\,a^{-1}}$ (mean value ± standard deviation), corresponding to a surface lowering of $-20 \pm 14\,\mathrm{m}$ between December 2010 and April 2021 (Fig. 3a). The maximum surface-lowering of $-56.9 \pm 0.1\,\mathrm{m}$ (or $-5.5 \pm 0.1\,\mathrm{m\,a^{-1}}$) of the same time period is evident in a graben-like structure in the center of the grounding line (Fig. 3a). This remarkable area of enhanced lowering is located downstream of a supraglacial lake and extends from $4\,\mathrm{km}$ upstream to $4\,\mathrm{km}$ downstream of the grounding line. Its width decreases in flow direction from a maximum of $1\,\mathrm{km}$ roughly $2\,\mathrm{km}$ upstream from the grounding line (Fig. 1c). While a hill was present in the ice surface in the central part near to and upstream of the grounding line until 2015, this turned into a depression (Fig. 3b,c) due to enhanced surface lowering rates compared to those rates outside the graben-like structure (Fig. 3e,f). The average elevation change upstream of the grounding line was $-2.1 \pm 0.1\,\mathrm{m\,a^{-1}}$ between December 2010 and April 2015 and has increased to $-6.6 \pm 0.1\,\mathrm{m\,a^{-1}}$ until the end of the time series in April 2021 (Fig. 3b,e). Outside this area, the surface lowered at a significantly smaller rate of $-1.1 \pm 0.1\,\mathrm{m\,a^{-1}}$. Further downstream where the ice is freely floating, this sink already existed in 2010 and the lowering rate was smaller (Fig. 3d,g). At both locations downstream from the grounding line, the (Eulerian) surface elevation change rate suddenly changed in late 2019 and became less strong (Fig. 3f) and even turned into thickening (Fig. 3g), similar to what we have observed until 2013.

In order to investigate what causes this drop in surface elevation, we recorded flight profiles with the UWB airborne radar. Near the grounding line, these airborne radargrams reveal the existence of several subglacial channels (Figs. 4 and Appendix Figs. C1 and C2). The by far largest channel with a height of $500\,\mathrm{m}$ and a width of $1\,\mathrm{km}$ is found in the central flow line near the grounding line and extends $5\,\mathrm{km}$ upstream from the grounding line. Above this channel, only $190\,\mathrm{m}$ of ice is left, which is 30% of the surrounding ice thickness. The location of this channel is in good agreement with the lowering of the surface observed from TanDEM-X satellite data (Fig. 3). However, upstream from the grounding line, the tip of the basal channel is located up to $400\,\mathrm{m}$ in the northwestern direction from the center of the surface depression. Between 2018 and 2021, the channel has grown especially in the upstream area, where the channel height has increased by almost $200\,\mathrm{m}$ (Fig. 4a,b). In contrast, no significant change in ice thickness or channel height occurred downstream of the grounding line (Fig. 4c). Seismic measurements from 1998 conducted by Mayer et al. (2000) show no indication of a channel existing at the base of 79NG (Fig. 4d). The ice has also thinned considerably outside the central channel. Along an across ice flow profile $600\,\mathrm{m}$ downstream from the grounding line, the average ice thickness in 2021 was $38\,\mathrm{m}$ less than in 2018 (Fig. 4c). Compared to 1998, the ice thickness $5\,\mathrm{km}$ downstream from the grounding line has even decreased by more than $230\,\mathrm{m}$ or 42%, which corresponds to a rate of $10\,\mathrm{m\,a^{-1}}$. The maximum thinning of 80% took place above the subglacial channel.

https://doi.org/10.5194/egusphere-2023-1320
Preprint. Discussion started: 28 July 2023

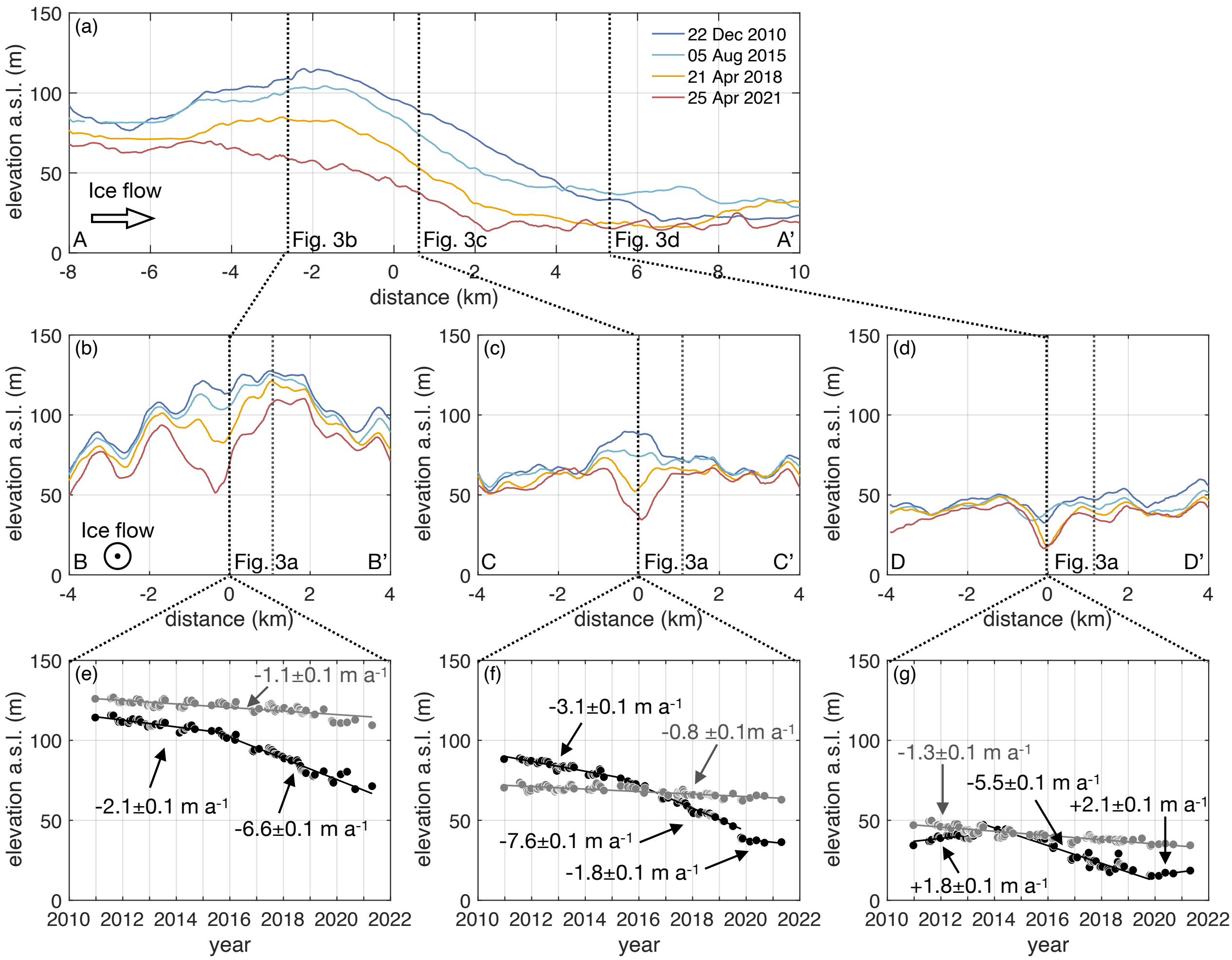

Figure 3. Surface elevation above sea level (EGM2008) from TanDEM-X satellite data between 2010 and 2021 (a) in ice flow direction and (b–d) across ice flow direction. The distance in (a) is relative to the grounding line and in (b–d) relative to the profile in (a). The location of all profiles is shown in Fig. 1 and here marked by dashed lines. (e–f) Time series of surface elevation since 2010 at the three crossings above (black) and outside (gray) the graben-like structure. The numbers represent the gradient of the linear regression.

https://doi.org/10.5194/egusphere-2023-1320
Preprint. Discussion started: 28 July 2023

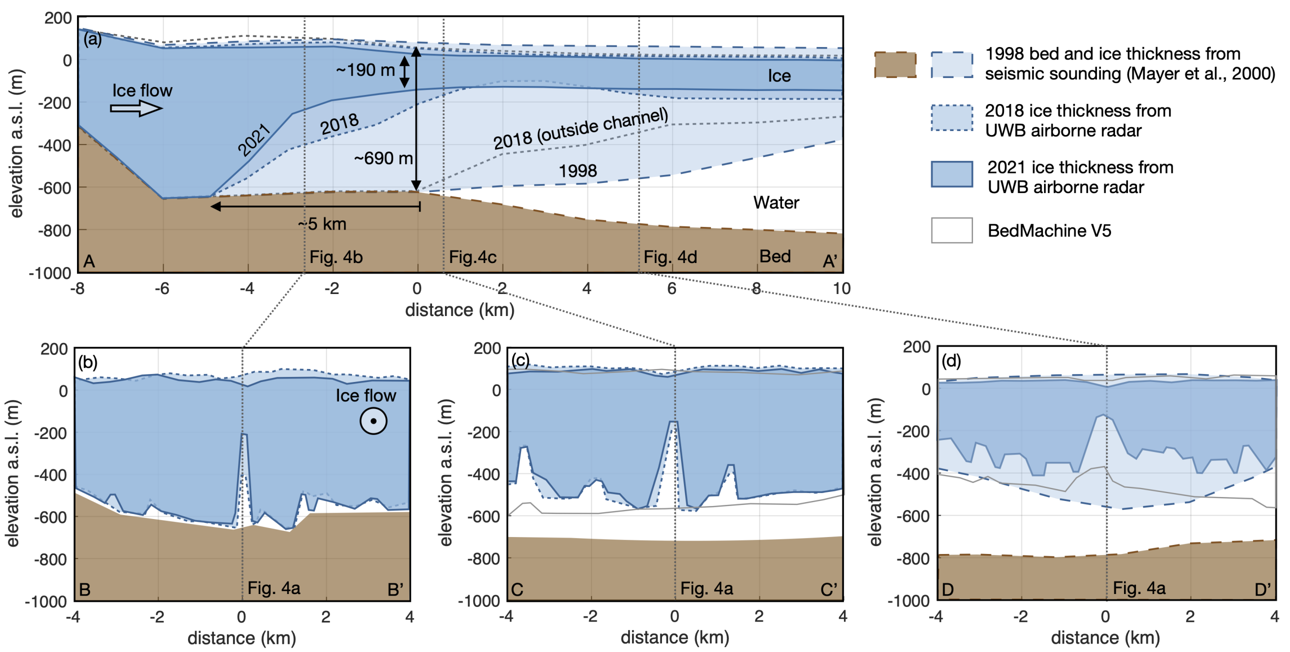

Figure 4. Sketch of the 79NG ice thickness between 1998 and 2021 (a) in ice flow direction and (b–d) across ice flow. The sketch in (a) and (d) is based on active seismic measurements by (Mayer et al., 2000) from 1998 and UWB airborne radar measurements from 2018 and 2021. The distance in (a) is relative to the grounding line and in (b–d) relative to the profile in (a). The locations of all profiles are shown in Fig. 1 and here marked by dashed lines. Fig. 3 shows the surface elevation change above these profiles. Appendix C shows the data this sketch is based on.

https://doi.org/10.5194/egusphere-2023-1320
Preprint. Discussion started: 28 July 2023

4.2 Extreme subglacial melting at the floating ice tongue

An analysis of the change in ice thickness at a given location (Eulerian perspective), as in the previous section, reveals changes in the geometry of the glacier. However, because the ice is flowing, considering the Lagrangian perspective is necessary for a full understanding of the process that causes these changes. The repeat UWB profile D–D' from July 2021 is the Lagrangian repeat of the profile C–C' from April 2018. On average, the ice thickness at profile D–D' in 2021 was reduced by $193\,\mathrm{m}$, corresponding to a mean annual rate of $59\,\mathrm{m\,a^{-1}}$. Since the surface ablation is typical $< 2\,\mathrm{m\,a^{-1}}$ (Zeising et al., 2020) and the dynamic thinning due to strain is small (Appendix B2), most of this thinning is attributed to basal melting.

In order to investigate the spatial distribution of Lagrangian thinning, we analyzed pRES measurements performed in July 2017 and 2018 at the same surface point. Figure 1b shows the spatial distribution of the thinning rates of all repeated pRES measurements (colored dots), while these are separated in Figure 1c into nadir (colored dots with a line showing the flow path) and off-nadir thinning rates (colored area). The marker shape of the off-nadir thinning rates corresponds to the scattering area from where the off-nadir basal reflections could have occurred. The thinning rates are between 1.7 ± 0.1 and $134 \pm 21\,\mathrm{m\,a^{-1}}$ for locations spread over the entire ice tongue of 79NG (Fig. 5). The highest (off-nadir) thinning rates of 126 ± 20 and $134 \pm 21\,\mathrm{m\,a^{-1}}$ were found at the most downstream bulge of the grounding line, next to the central subglacial channel where the ice draft is large. However, moderate thinning rates of $< 21\,\mathrm{m\,a^{-1}}$ were observed at a similar distance to the grounding line and for a similar draft (Fig. 5). Further downstream, but still within the hinge zone, we observed predominantly high thinning rates ($> 50\,\mathrm{m\,a^{-1}}$) spread across the entire width of the ice tongue. In general, thinning rates are observed to be below $30\,\mathrm{m\,a^{-1}}$ several kilometers downstream from the grounding line, declining towards the calving front to between 1.7 ± 0.1 and $3.2 \pm 0.1\,\mathrm{m\,a^{-1}}$ (Figs. 1 and 5).

Variability on small spatial scales is accessible using a combination of nadir and off-nadir returns. At the pRES measurement location g4_p02 (Fig. 2), where we link the origin of the off-nadir reflection to a small subglacial channel, we derived two estimates of thinning rates: One is based on the repeated nadir reflection outside the channel ($6.4 \pm 0.1\,\mathrm{m\,a^{-1}}$) while the other is based on both first basal (off-nadir) reflections in 2017 and 2018 within the channel ($73 \pm 10\,\mathrm{m\,a^{-1}}$). This comparison indicates a growth of the subglacial channel by more than $66\,\mathrm{m\,a^{-1}}$.

The ApRES time series show a strong spatial and temporal variability of basal melt rates without a clear seasonal cycle. All three ApRES recorded high melt rates between October 2017 and July 2018 of $> 50\,\mathrm{m\,a^{-1}}$ on average, which reduced to $\sim 30\,\mathrm{m\,a^{-1}}$ until April 2019 and stayed low until the end of the record in July 2022 (Fig. 6). This change is particularly pronounced at ApRES1, which is located on the southeastern side of the glacier. Between April 2018 and April 2019, when ApRES1 was about $8 – 9\,\mathrm{km}$ downstream from the grounding line, the melt rate dropped from $137 \pm 2\,\mathrm{m\,a^{-1}}$ (95% quantile) to just $30 \pm 1\,\mathrm{m\,a^{-1}}$ (Fig. 6a). After two periods with higher melt in summer and autumn 2020, the basal melt rate reduces to zero for almost all of the remaining 18 months. In early 2017, melt rates $> 120\,\mathrm{m\,a^{-1}}$ (95% quantile) were recorded $5.5\,\mathrm{km}$ downstream from the grounding line at the north-western side by ApRES2a at the first basal return, whereas at the same time, the median melt rate was below $50\,\mathrm{m\,a^{-1}}$ (Fig. 6b). After the relocation of ApRES2a (now named ApRES2b) to its starting point in the summer of 2018, ApRES2b recorded a $50\,\mathrm{m}$ lower ice thickness and a 50% lower melt rate (95% quantile) than

https://doi.org/10.5194/egusphere-2023-1320
Preprint. Discussion started: 28 July 2023

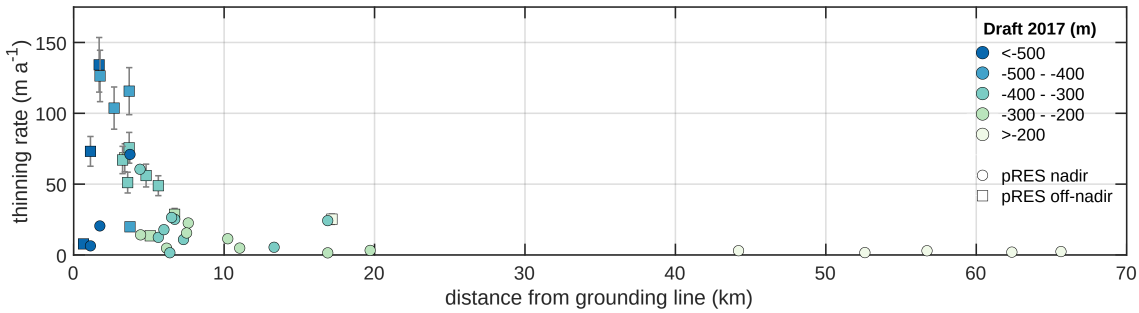

Figure 5. Distribution of the thinning rate as a function of distance from the grounding line. Color-coded draft of the floating tongue derived from pRES measurements and separated for nadir and off-nadir thinning rates. Most uncertainties are too small to visualize.

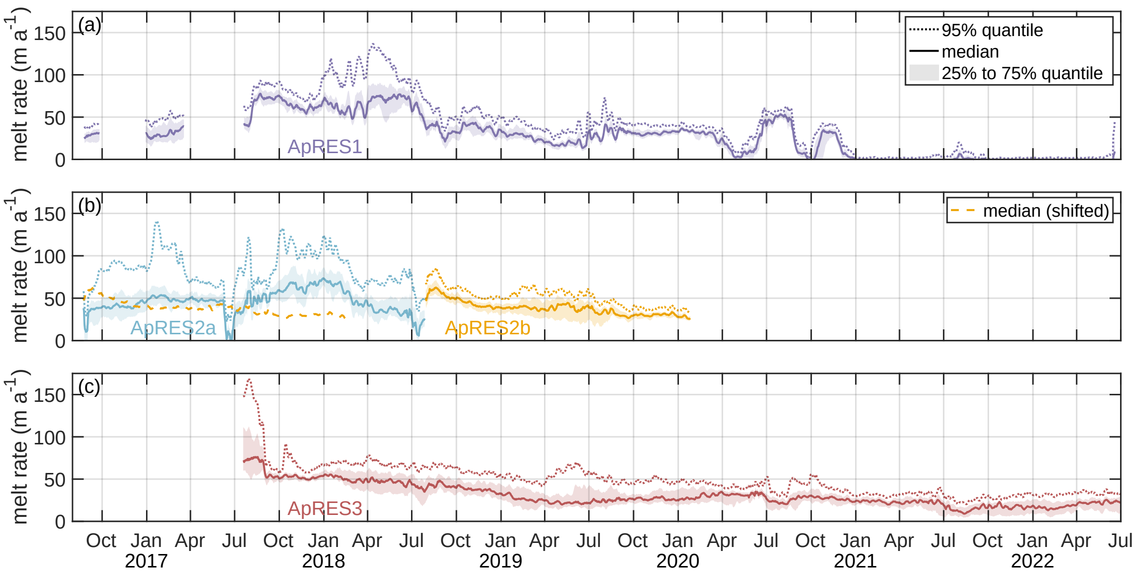

Figure 6. Basal melt rate time series of all ApRES measurements: (a) ApRES1, (b) ApRES2a and ApRES2b, (c) ApRES3. The dashed line shows the 95% quantile, the solid line the median, and the shaded area marks the range between the 25% and 75% quantile. The dotted line in (b) represents the mean melt rate of ApRES2b shifted in time for a comparison with ApRES2a from an Eulerian perspective.

ApRES2a two years before. Furthermore, the spatial variability (difference between the median and 95% quantile) of ApRES2b was greatly reduced. The highest melt rates of $150 – 168 \pm 5\,\mathrm{m\,a^{-1}}$ lasting $17\,\mathrm{d}$ were recorded at ApRES3 at the beginning of the time series in July and August 2017. At that time, the ApRES3 was located $3\,\mathrm{km}$ from the grounding line next to the large central basal channel. After these high melt rates dropped to roughly $50\,\mathrm{m\,a^{-1}}$ after the summer in 2017, the basal melt rate showed, in general, a steady decrease to $\sim 20\,\mathrm{m\,a^{-1}}$ until the end of the time series in July 2022.

https://doi.org/10.5194/egusphere-2023-1320
Preprint. Discussion started: 28 July 2023

5 Discussion

An analysis of the change in 79NG's geometry between 1998 (Mayer et al., 2000) and 2021 (this study) reveals a thinning by 42% and an ice base that became channelized, especially in the vicinity of the grounding line (Fig.4d). Compared to the 30% thinning observed by Mouginot et al. (2015) for the period 1999 to 2014, the thinning has continued without accelerating. The onset of steep basal slopes has been shifted several kilometers in the upstream direction, especially within the large central channel (Fig.4a). We associate this shift with enhanced basal melt rates that are above those required for a steady-state ice thickness and thus causing steep basal gradients. A remarkably similar change in geometry was found for a melt channel at Petermann Glacier between 2002 and 2010 (Münchow et al., 2014). For the initialization of ice sheet models, ice geometries such as the one from BedMachine (Morlighem et al., 2017) are often used, which are based on a compilation of airborne radar measurements. At 79NG, ice thickness measurements since 1993 have been taken into account in BedMachine V5 (Morlighem et al., 2022), also the 2018 UWB data have been included here. The comparison of the 2021 UWB ice thicknesses with BedMachine V5 at the two across-ice flow sections C–C' and D–D' shows differences of $-91 \pm 108\,\mathrm{m}$ and $-188 \pm 56\,\mathrm{m}$, respectively (Fig. 4c,d). This illustrates that the ice thickness is difficult to represent of those glaciers which change significantly in a few years due to the warming of the ocean and atmosphere. The impact of a more accurate, current ice thickness distribution on the simulated evolution of floating ice tongues needs to be explored in regional studies such as the one from Choi et al. (2017) for 79NG, which is beyond the scope of this study.

At Petermann Glacier, Washam et al. (2019) observed strong seasonal variations of basal melt rates beneath the floating tongue with summer melt rates more than four times larger than in winter. They linked the seasonality to warmer ocean currents reaching the ice base of Petermann Glacier (Shroyer et al., 2017; Washam et al., 2019). In contrast to this, we see no evidence of seasonality in the melt rate time series for 79NG, despite the increase in melting at ApRES1 in July 2020. The absence of a summer increase of basal melt rates is consistent with in-situ measurements of ocean temperatures and velocities between September 2016 and September 2017 (Schaffer et al., 2020), showing persistent inflow of warm AIW into the cavity and an overlying outflow of cold-modified AIW throughout the year without a clear seasonal signal. Also, the calving front position of 79NG shows no pronounced seasonality (Loebel et al., 2023).

Combining the findings of this study with the observed inflow (Schaffer et al., 2020) and modeled (Reinert et al., 2023) currents below the 79NG shapes a full picture of the ice–ocean interaction at 79NG. Warm AIW flows over the sill into the cavity as a dense and saline bottom plume. As the keel of thick ice near the grounding line is exposed to this warm water, large amounts of heat are supplied to the ice base, which results in the observed high thinning and melt rates (see Appendix D). The meltwater rises along the basal slope as a positively buoyant plume that may drive turbulent mixing with the warm AIW and thus intensify basal melting (Jenkins and Doake, 1991; Jenkins, 2011; Schaffer et al., 2020).

The spread of thinning rates near the grounding line from near zero to $> 100\,\mathrm{m\,a^{-1}}$ may be related to the water column thickness distribution. A water column thickness of 50 to $140\,\mathrm{m}$ (Mayer et al., 2000) was found where we observe the highest basal melt rates and where the grounding line reaches farthest downstream. We do not have any information on water column thickness elsewhere. However, the southeastern part of the grounding line is situated on a mountainous landform. We hypoth-

https://doi.org/10.5194/egusphere-2023-1320
Preprint. Discussion started: 28 July 2023

esize that only a shallow water column exists here, which prevents the flow of warm ocean currents toward the grounding line, resulting in the observed low thinning rates. Further downstream, the plume loses heat to the melting of ice and buoyancy by entrainment of ambient water. Thus, it cools down and eventually detaches from the ice base, leading to a strong decrease in basal melting for the thinner, more gently sloped areas of the floating ice tongue (Reinert et al., 2023). This concept is consistent with the low melt rates and glacially modified AIW observed at the calving front, where the outflowing water is $0.9\,^{\circ}\mathrm{C}$ cooler than the inflowing AIW (Schaffer et al., 2020).

While this picture accounts for the first-order, quasi-twodimensional distribution of melt rates as well as the observed hydrography, it does not explain the existence and growth of basal channels. In previous studies, the existence and location of basal channels have been linked to subglacial water discharge that rises along the basal slope inside a pre-existing basal channel and intensifies basal melting (Le Brocq et al., 2013; Marsh et al., 2016; Washam et al., 2019). We hypothesize that the same applies to the large basal channel at 79NG, where subglacial discharge might have caused the channel's growth in the upstream direction due to extreme basal melting. Although there are no measurements of basal melt rates within the channel, we can draw conclusions about them by considering the basal geometry and its changes in time. Thus, the high melt rates occur primarily near the origin of the channel, where the greatest basal slope exists. With decreasing basal slopes inside the channel, the melt rate also decreases. This results in an upstream shift in the melt pattern compared to the outside of the channel: (i) Upstream the grounding line, higher melt rates occur inside the channel than outside where the ice is grounded or where a low water column exists. (ii) In the vicinity of the grounding line, lower melt rates occur in the channel than outside where the ice is in contact with warm ocean currents. This pattern is consistent with observations from a basal channel at the Filchner Ice Shelf, Antarctica (Humbert et al., 2022a). In addition, it explains the small-scale variability in melt rates we observe at some pRES measurement locations (e.g. at g4_p02 in Figs. 1c, 2).

The steepening of an ice base is indicating that the melt rates and the ice transport are not in equilibrium, which seems to be the case at 79NG in the past at the same time when the inflow of warm AIW was present. However, we found indications for reduced heat transport into the cavity of 79NG since 2018. In that year, we observed a strong decrease in the melt rate at all ApRES sites that remained low since. Additionally, the repeat of the ApRES2 measurements after two years shows that high melt rates between October 2016 and July 2018 have reduced the ice thickness at the starting location of the ApRES measurement by $50\,\mathrm{m}$ (Eulerian perspective). Due to the lower melt rates from July 2018 onward, the ice thinned less than before (Lagrangian perspective). As a result, the ice thickness at the location where the measurement of ApRES2b stopped in December 2019 was even thicker than two years before.

Besides a warm AIW inflow into the cavity, the melt rates can also be enhanced by an increase in subglacial discharge. It is to be expected that this mainly affects the melt rates in the basal channels (Le Brocq et al., 2013). This appears to have been the case for 79NG over the past decade as the central channel has grown and evolved in the upstream direction. In order to quantify if an increase in subglacial discharge has occurred, we roughly estimated the upstream extent of the average surface melt area from a simple analysis of the median summer skin temperatures (July and August) from the Copernicus Arctic Regional Reanalysis (Schyberg et al., 2020) along the ice flow line upstream of the large central channel (Figs. 7, E1). This revealed a substantial increase of the median temperature by up to $1.9\,^{\circ}\mathrm{C}$ since the year 2000. The area in which the temperature was

https://doi.org/10.5194/egusphere-2023-1320
Preprint. Discussion started: 28 July 2023

positive 50% of the days ranged $32\,\mathrm{km}$ upstream until the period 2000–2004, but over $70\,\mathrm{km}$ since 2005–2009. Thus, intense warming of the atmosphere in the early 2000s increased the area of summer surface melt and most likely increased subglacial discharge. This is consistent with the finding at Petermann Glacier, where the subglacial water discharge has doubled since 2001 (Ciracì et al., 2023).

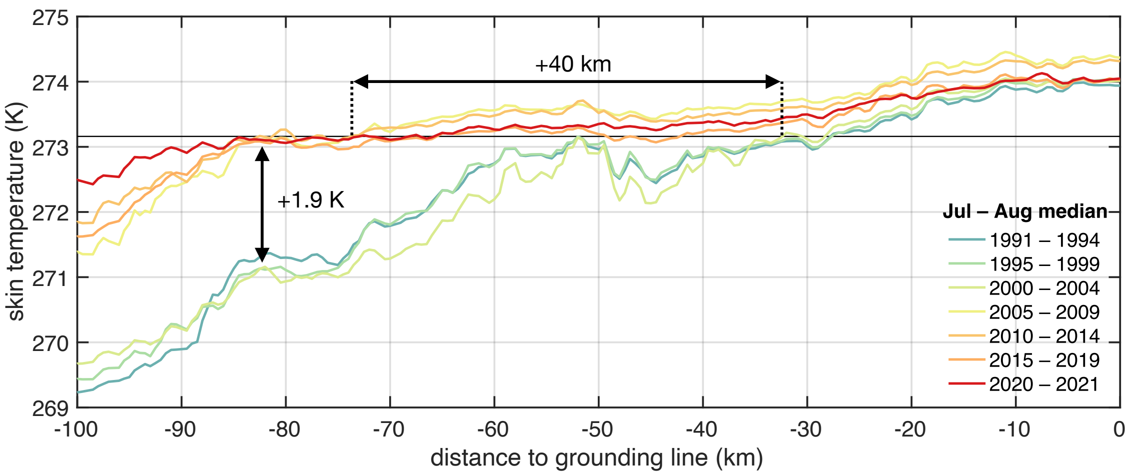

Figure 7. Development of skin temperature from Copernicus Arctic Regional Reanalysis (Schyberg et al., 2020) along the central flow line since 1991. The temperature shown is the median skin temperature between 01 July and 31 August (at 15:00 UTC) for the given years. Maps of the median skin temperature are shown in Appendix E.

6 Conclusions

By combining geophysical in-situ and remote sensing methods, we revealed changes in the ice geometry of the 79NG: the ice near the grounding line has become channelized and significantly thinner in the last two decades. Large, $500\,\mathrm{m}$ high subglacial channels originate several kilometers upstream of the grounding line. Here, higher melt rates occur inside the channel than outside, while downstream of the ground line we found evidence of higher melt rates outside the channels. These high melt rates of $> 100\,\mathrm{m\,a^{-1}}$ are caused by thick ice that is in contact with the warm bottom plume and result in steep basal slopes because they exceed such melt rates, which are necessary for a steady-state ice thickness. However, we also found low melt rates and small basal gradients under thick ice, particularly off the center, which we attribute to a shallow water column thickness that prevents the flow of warm ocean currents toward the grounding line. As the ice thins in the downstream direction, the basal slope and the melt rates drop sharply, resulting in low values at the calving front. The temporal variation since September 2016 shows a non-seasonal variability and significantly decreasing Lagrangian melt rates with increasing distance to the grounding line. Since 2018, these time series show a decrease in melt rates, suggesting a recent inflow of colder water into the cavity beneath the glacier. We conclude that warmer ocean inflow and increased subglacial discharge have caused the changes in

https://doi.org/10.5194/egusphere-2023-1320
Preprint. Discussion started: 28 July 2023

ice geometry in the vicinity of the grounding line by forcing high basal melt rates. The consequences of the thinning on the stability of the 79NG and the Northeast Greenland Ice Stream should be investigated in further studies.

Data availability. Time-series of basal melt rates, thinning rates derived from single repeated pRES measurements and ice thickness data from the 2021 UWB survey are submitted to the World Data Center PANGAEA. Stake surface ablation/accumulation measurements from 2017 to 2018 (https://doi.org/10.1594/PANGAEA.922131; Zeising et al., 2020) are available at the World Data Center PANGAEA.

https://doi.org/10.5194/egusphere-2023-1320
Preprint. Discussion started: 28 July 2023

Appendix A: Occurrence and identification of nadir and off-nadir reflection

We have identified different cases of how nearby basal channels affect the origin of the first recorded basal reflection in repeated pRES echograms (Tab. A1 and Fig. A1). All have in common that the derived range differences of two measurements (ΔR derived) underestimate the nadir ice thickness (ΔH nadir) or the off-nadir ice thickness (ΔH off-nadir).

Table A1. Possibilities of how basal channels affect the recording of nadir and off-nadir reflections. Notation: t_1: time of first measurement, t_2: time of repeated measurement, H_1: ice thickness at t_1, H_2: ice thickness at t_2, ΔH nadir: difference in ice thickness nadir, ΔH off-nadir: difference in ice thickness at off-nadir location, ΔH derived: difference in depth at nadir projection.

Case	Figure	t_1	t_2	ΔH
A	Fig. A1a	**nadir**	**off-nadir**	ΔH **nadir** $<$ ΔR **derived** $<$ ΔH **off-nadir**
		Basal channel did not exist or was too small to be detected at t_1. At t_2, the growth of the channel is significantly larger than the ice thickness reduction nadir of the measurement device.		
B	Fig. A1b	**off-nadir**	**off-nadir**	ΔR **derived** $<$ ΔH **off-nadir**
		Basal channel exists at t_1. At t_2, the ice thickness reduction nadir of the measurement device is not significantly larger than the growth of the channel.		
C	Fig. A1c	**off-nadir**	**nadir**	ΔH **off-nadir** $<$ ΔR **derived** $<$ ΔH **nadir**
		Basal channel exists at t_1. At t_2, the ice thickness reduction nadir of the measurement device is significantly larger than the growth of the channel.		
D	Fig. A1d	**off-nadir**	**off-nadir**	ΔR **derived** $<$ ΔH **off-nadir**
		Two basal channel exist at t_1. At t_2, the ice thickness reduction nadir of the measurement device is not significantly larger than the growth of at least one of both channels. This type can not be distinguished from Case B with simple measurements.		

Several pRES echograms indicate the occurrence of numerous strong basal reflections (Fig. A2). For steep basal gradients, the off-nadir reflection may occur prior to the nadir reflection. We interpret the first basal reflection as an off-nadir reflection, as long as no further information reveals the true nadir reflection. Herewith, the resulting basal melting in the vicinity of the measurement is always underestimated, although the nadir melt rate might be lower.

https://doi.org/10.5194/egusphere-2023-1320
Preprint. Discussion started: 28 July 2023

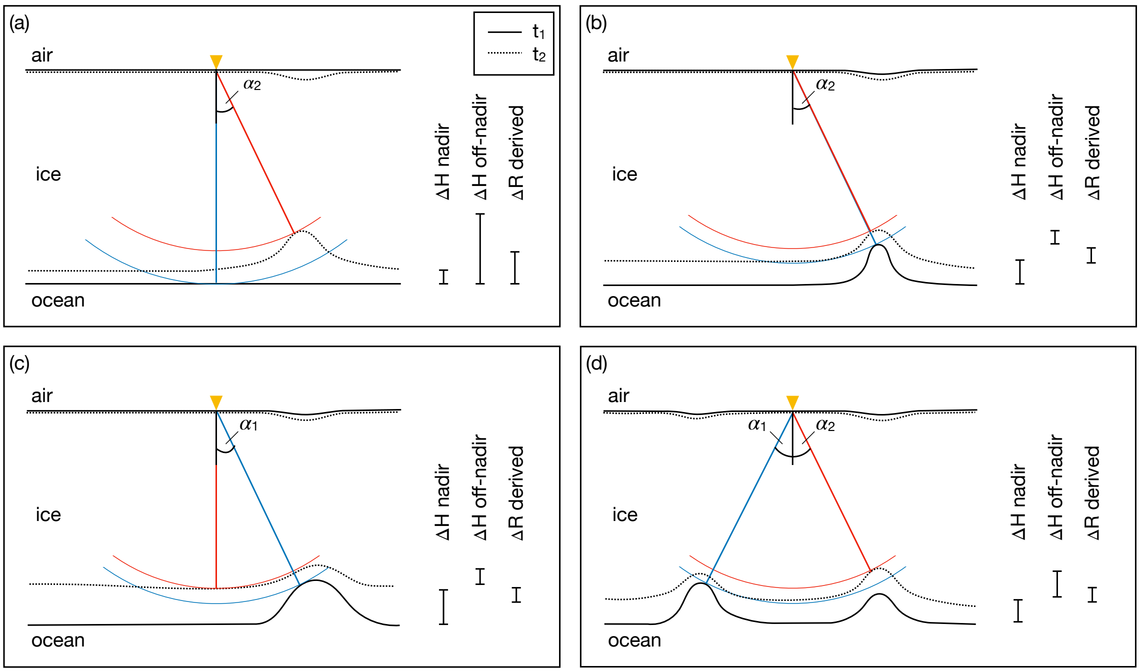

Figure A1. Sketch of off-nadir reflections and their influence on basal melt rates. The solid lines refer to the time of the first measurement (blue), t_1, and the dotted lines refer to the time of the repeat measurement (red), t_2. The yellow triangles mark the measurement positions. The red and blue straight lines mark the closest distance from the measurement to the ice base. The segments of a circle (up to 30° to nadir) correspond to the possible positions of the reflector with the shortest distance. The lengths of the bars on the right reflect the thinning of the ice between t_1 and t_2 for the position of the measurement (ΔH nadir), for the position of the closest reflector at t_2 (ΔH off-nadir), and for the range difference of the blue and red lines (ΔR derived). Note that at least one of ΔH nadir or ΔH off-nadir is always larger than ΔR derived.

https://doi.org/10.5194/egusphere-2023-1320
Preprint. Discussion started: 28 July 2023

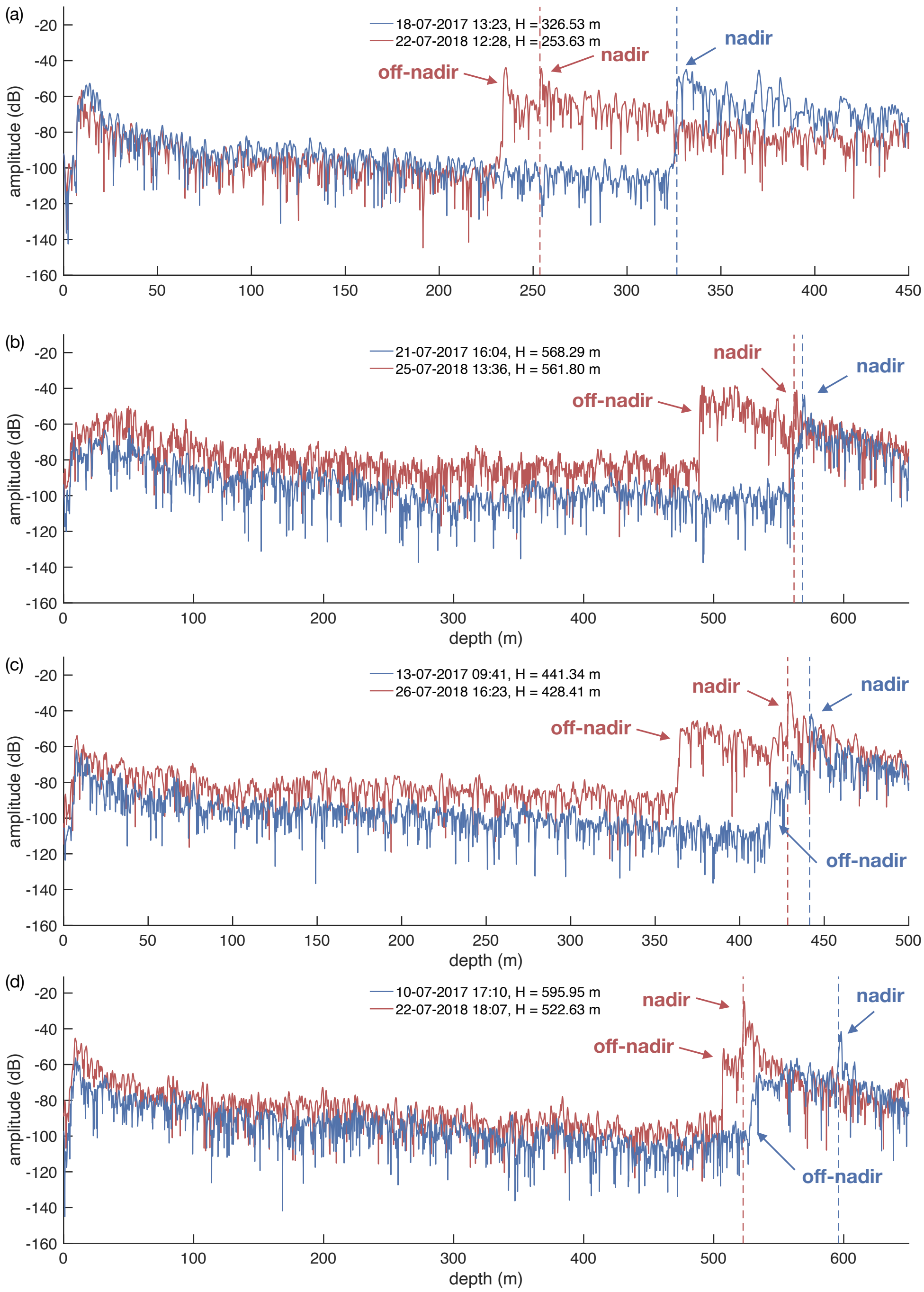

Figure A2. pRES measurements with the identified nadir and off-nadir reflections. Echograms from the first measurement are shown in blue and from the repeated measurement in red. Vertical dashed lines mark the nadir basal return and thus represent the ice thickness H.

https://doi.org/10.5194/egusphere-2023-1320
Preprint. Discussion started: 28 July 2023

Appendix B: ApRES time series analysis

B1 Estimation of ice deformation

Ice deformation affects the range R from the ApRES to an englacial reflector located at x_0, y_0, and z_0 relative to the measurement location. ApRES measurements allow us to determine the depth profile of the vertical displacement of englacial reflectors relative to the surface and thus to compute the vertical strain ε_{zz}. The range displacement of an off-nadir reflector viewed at an angle α due to ice deformation ΔR_ε is also affected by the two horizontal normal ε_{xx} and ε_{yy} as well as the shear components ε_{xz}, ε_{yz}, ε_{zx} and ε_{zy}. Accordingly, the location of a reflector shifts to $x_0 + \int_0^{x_0} (\varepsilon_{xx} + \varepsilon_{xz})\,\mathrm{d}x$, $y_0 + \int_0^{y_0} (\varepsilon_{yy} + \varepsilon_{yz})\,\mathrm{d}y$ and $z_0 + \int_0^{z_0} (\varepsilon_{zz} + \varepsilon_{zx} + \varepsilon_{zy})\,\mathrm{d}z$ at the time of a second measurement so that ΔR_ε can be calculated as follows:

$$\Delta R_\varepsilon = \sqrt{\left(x_0 + \int\limits_0^{x_0} (\varepsilon_{xx} + \varepsilon_{xz})\,\mathrm{d}x\right)^2 + \left(y_0 + \int\limits_0^{y_0} (\varepsilon_{yy} + \varepsilon_{yz})\,\mathrm{d}y\right)^2 + \left(z_0 + \int\limits_0^{z_0} (\varepsilon_{zz} + \varepsilon_{zx} + \varepsilon_{zy})\,\mathrm{d}z\right)^2} - \sqrt{x_0^2 + y_0^2 + z_0^2} \tag{B1}$$

For a nadir reflection ($\alpha = 0$) where $x_0 = 0$ and $y_0 = 0$, the displacement due to deformation depends only on the vertical strain

$$\Delta R_\varepsilon^{\mathrm{n}} = \int\limits_0^{z_0} \varepsilon_{zz}\,\mathrm{d}z, \tag{B2}$$

where the range R and thus z_0 equals the ice thickness H.

The estimation of ΔR_ε in the case of an off-nadir reflection requires the quantification of the normal and shear components as well as of α and β, which are unknown. In the following, we consider the shear terms to be small, as investigation of a melt channel on Filchner Ice Shelf (Humbert et al., 2022a) has shown that the elastic shear strain is an order of magnitude lower than the strain in normal direction. With channels appearing during our measurement period, the instantaneous elastic component is the one to be considered here. From the continuity equation (e.g. Cuffey and Paterson, 2010), we find that

$$\varepsilon_{zz} = -(\varepsilon_{xx} + \varepsilon_{yy}) \tag{B3}$$

which is the case for incompressible ice. Additionally, we know that $\alpha \leq 30°$ for the ApRES system so that the sum of the horizontal distances between the ApRES and the reflector is smaller or equals the vertical distance: $x_0 + y_0 \leq z_0$. Thus, we can do the following quantification

$$0 \leq |\Delta R_\varepsilon| \leq |\Delta R_\varepsilon^{\mathrm{n}}|, \tag{B4}$$

where ΔR_ε and $\Delta R_\varepsilon^{\mathrm{n}}$ have always the same sign. This shows that strain thinning or thickening cannot be overestimated by assuming a reflection occurred from a nadir scatterer.

https://doi.org/10.5194/egusphere-2023-1320
Preprint. Discussion started: 28 July 2023

B2 ApRES echograms

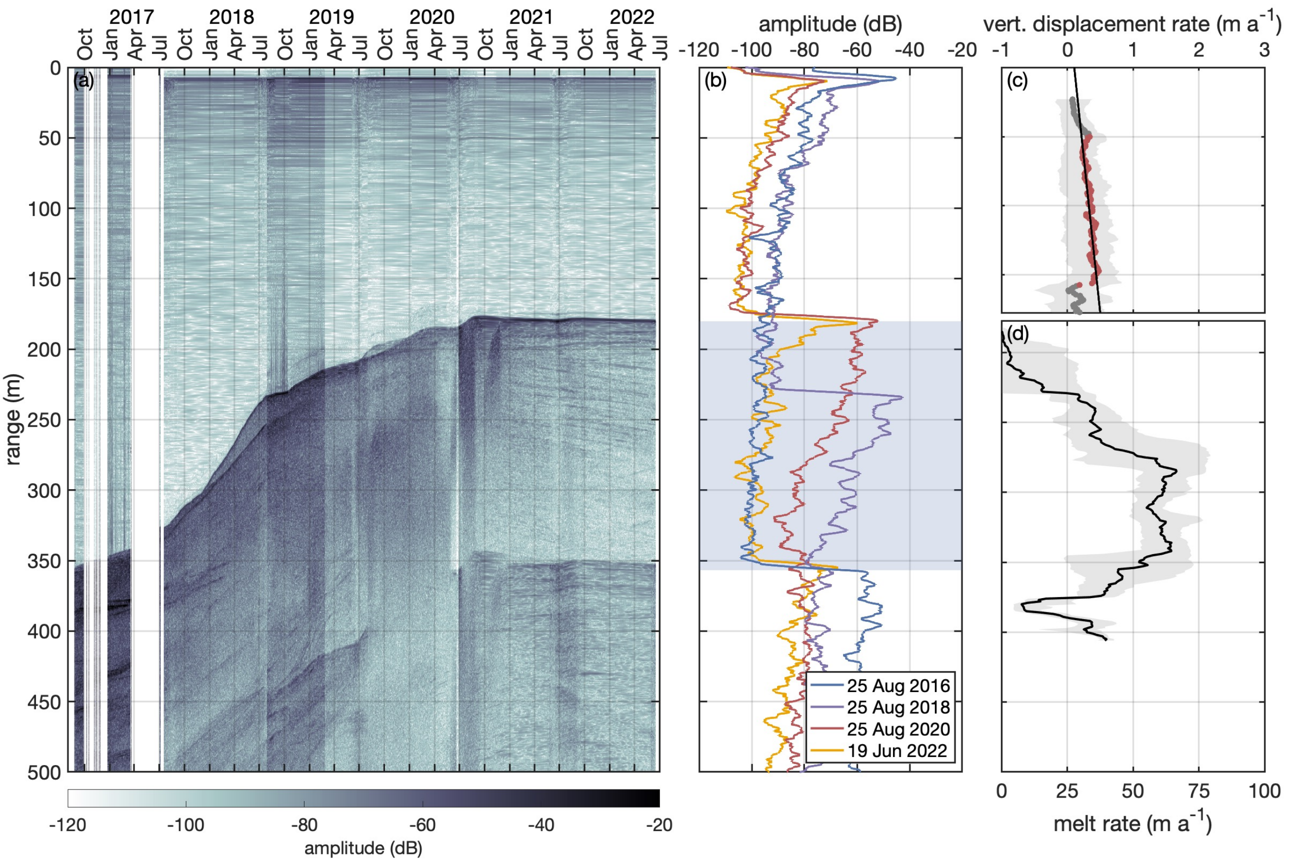

Figure B1. Analysis of ApRES1 echograms. (a) Time-echogram of a Lagrangian measurement at ApRES1 recorded between August 2016 and June 2022. In 2016 and 2017, several ApRES malfunctions caused data gaps. (b) Selected echograms smoothed with a 5 m moving average filter. The blue-shaded range corresponds to the displacement of the first basal return within the measurement period. (c) Mean vertical displacement of englacial segments (dots). The gray shaded area marks the range between the 25% and 75% quantile. Segments between 20 m and 20 m above the first basal return at the end of the measurement period (red dots) were used to calculate the change in ice thickness due to vertical strain by fitting a linear function (black line). (d) Average melt rate of the corresponding depth (black line). The gray shaded area marks the range between the 25% and 75% quantile.

https://doi.org/10.5194/egusphere-2023-1320
Preprint. Discussion started: 28 July 2023

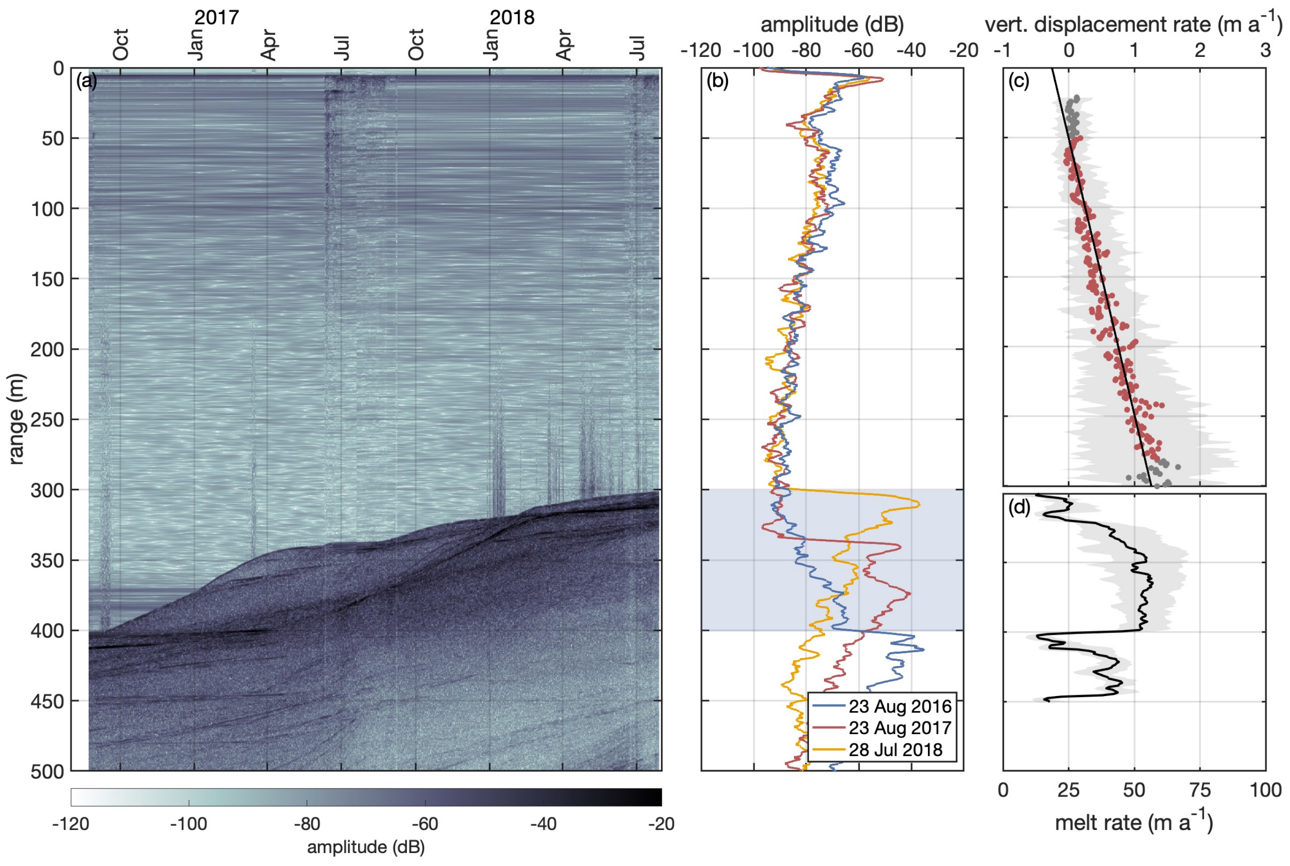

Figure B2. Same as Figure B1 but for ApRES2a.

https://doi.org/10.5194/egusphere-2023-1320
Preprint. Discussion started: 28 July 2023

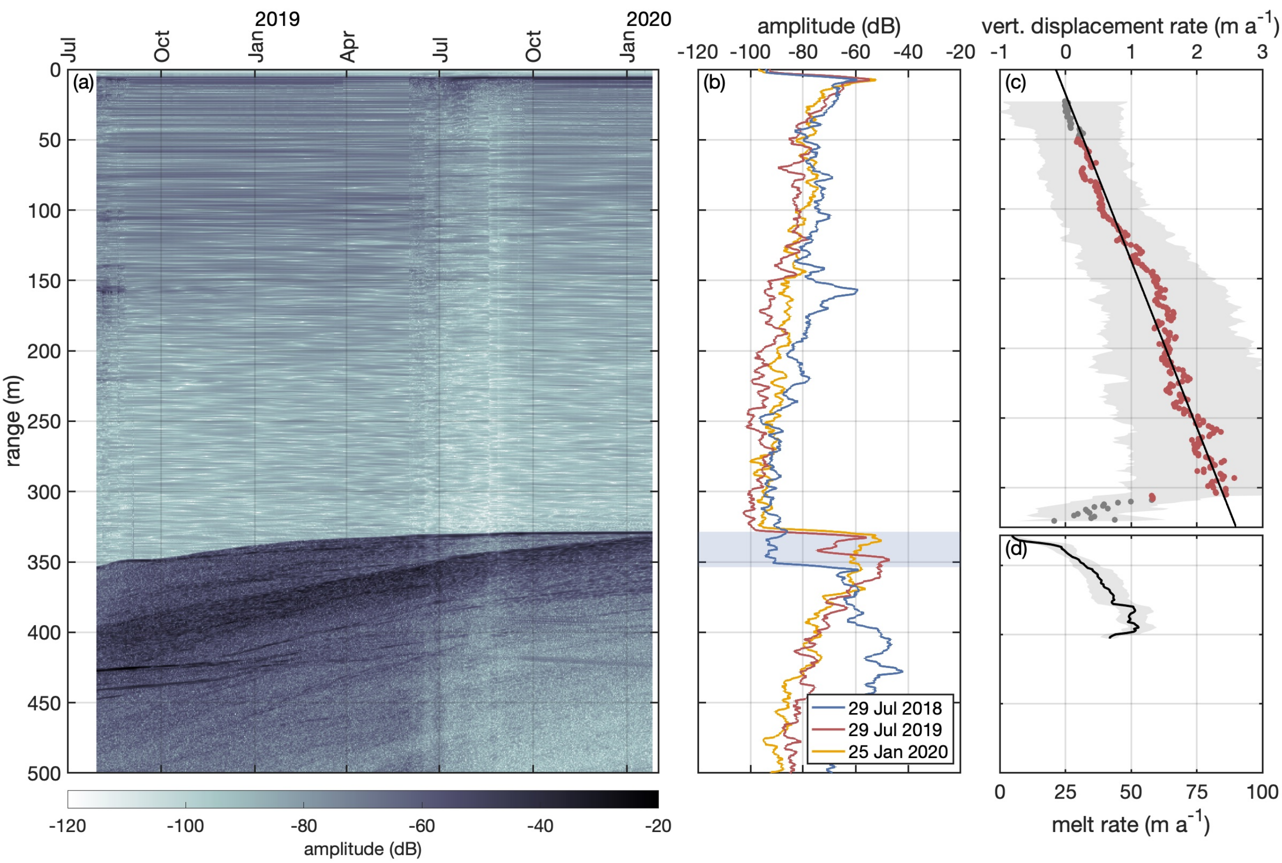

Figure B3. Same as Figure B1 but for ApRES2b.

https://doi.org/10.5194/egusphere-2023-1320
Preprint. Discussion started: 28 July 2023

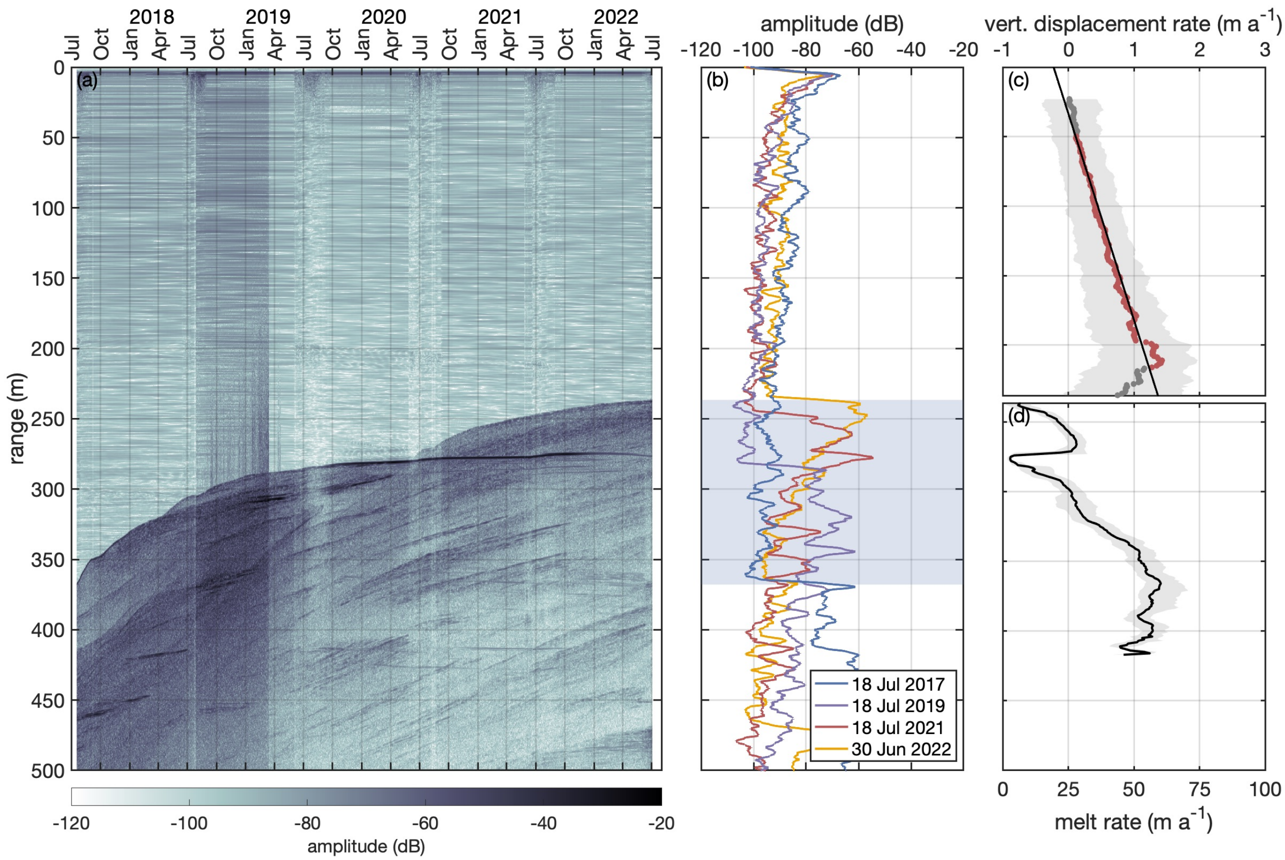

Figure B4. Same as Figure B1 but for ApRES3.

https://doi.org/10.5194/egusphere-2023-1320
Preprint. Discussion started: 28 July 2023

Appendix C: Subglacial channel observed by airborne radar

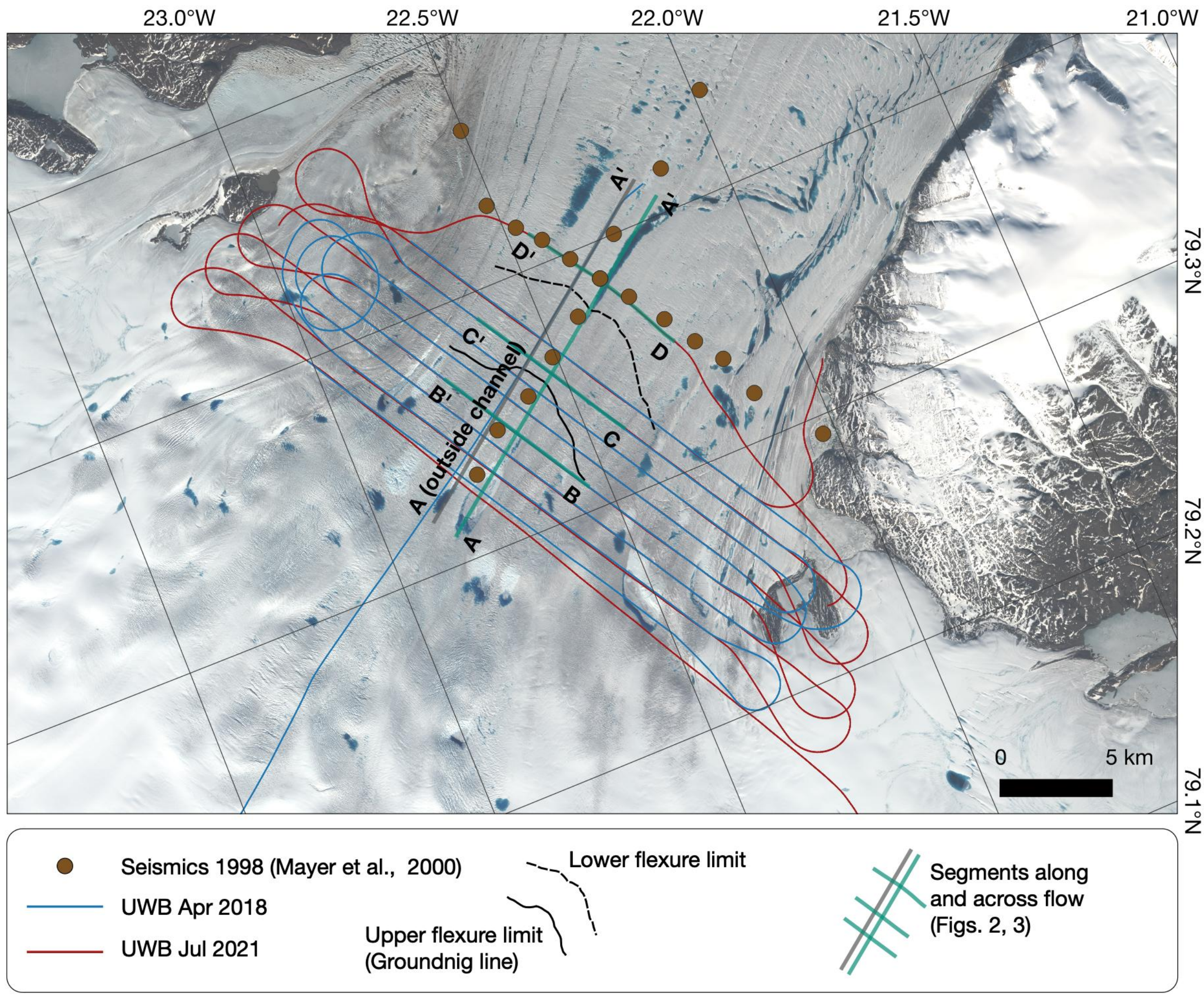

Figure C1. Map of UWB airborne radar data from 2018 and 2021 and seismic locations from 1998 (Mayer et al., 2000).

https://doi.org/10.5194/egusphere-2023-1320
Preprint. Discussion started: 28 July 2023

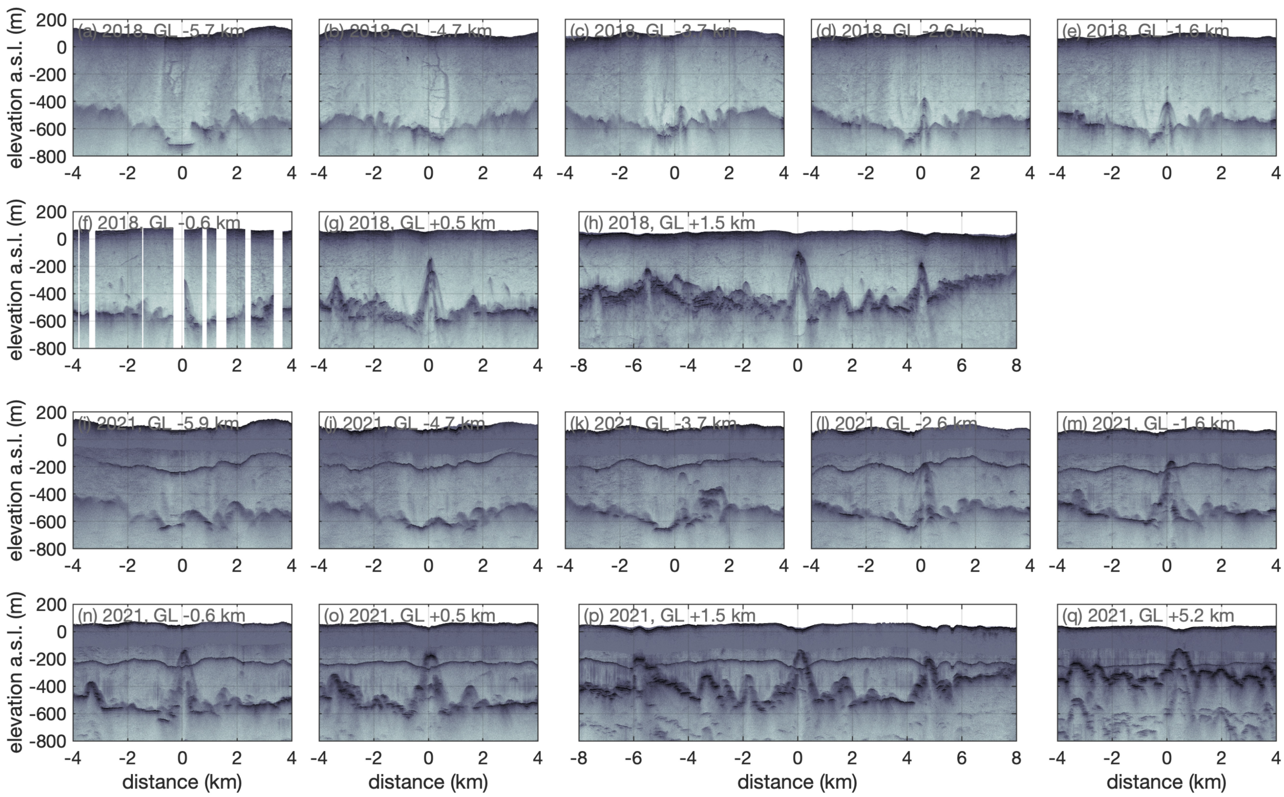

Figure C2. UWB airborne echograms across basal channel (a–h) from 2018 and (g–q) from 2021. For location see Fig. C1.

https://doi.org/10.5194/egusphere-2023-1320
Preprint. Discussion started: 28 July 2023

Appendix D: Oceanic heat flux

In order to estimate the oceanic heat flux q_w required to sustain the basal melt rates a_b $[\mathrm{m\,s^{-1}}]$ derived in this study, we separate the heat flux q_w into two components: the heat flux q_m to melt the ice and the heat flux into the glacier interior q_i that is required for heating the ice by ΔT to the pressure melting point:

$$q_w = \underbrace{\rho_i\, a_b\, L}_{q_m} + \underbrace{\rho_i\, c_i(T)\, a_b\, \Delta T}_{q_i} \tag{D1}$$

The heat fluxes depend on the density of the ice, $\rho_i = 917\,\mathrm{kg\,m^{-3}}$, the latent heat of fusion, $L = 334000\,\mathrm{J\,kg^{-1}}$, and the specific heat capacity for ice, $c_i(T) = 146.3 + 7.253 \cdot T[\mathrm{K}]\,\mathrm{J\,kg^{-1}\,K^{-1}}$ with the temperature T in Kelvin (Ritz, 1987). For an assumed range of glacier interior temperatures between $\sim 0\,\mathrm{K}$ (temperate ice) and $30\,\mathrm{K}$ below the pressure melting point, a basal melt rate of $140\,\mathrm{m\,a^{-1}}$ (as it was observed at all three ApRES sites) requires a heat flux between 1360 and $1600\,\mathrm{W\,m^{-2}}$. This heat flux must be provided by the water in the cavity below 79NG.

To obtain an estimate of the oceanic heat flux, we follow the approach implemented in the Finite Element Sea ice-Ocean Model (FESOM; Timmermann et al., 2012). Here, a three-equation system is used that determines the temperature and salinity of a thin boundary layer along the ice-shelf base from its heat and freshwater exchange with the ice and the ambient ocean (Hellmer and Olbers, 1989; Holland and Jenkins, 1999). Besides the ocean temperature, the heat flux into this boundary layer is determined by the flow velocity in the ambient ocean, as the latter determines the friction and thus defines the turbulent fluxes of heat and salt (Jenkins and Doake, 1991).

As an example case for the 79NG sub-ice cavity, we assume a salinity of $34.5\,\mathrm{psu}$ and an ice draft of $320\,\mathrm{m}$, estimated for the location of ApRES2a, where the highest melt rates of $140\,\mathrm{m\,a^{-1}}$ were determined during winter. Measurements of the inflow temperatures exceed $1.2\,^\circ\mathrm{C}$ at the calving front (Schaffer et al., 2020), corresponding to $2.9\,\mathrm{K}$ above the pressure melting point at the position of the observation. In order to produce a sufficiently high turbulent heat flux into the boundary layer for this given temperature, an ambient velocity of $0.22\,\mathrm{m\,s^{-1}}$ is required for temperate ice and $0.27\,\mathrm{m\,s^{-1}}$ for ice of $30\,\mathrm{K}$ below the pressure melting point. Previously simulated velocities of a buoyant plume rising along the ice base of 79NG indicate velocities of up to $0.22\,\mathrm{m\,s^{-1}}$ (Reinert et al., 2023). From these numbers, we conclude that the ocean currents underneath 79NG are able to supply a heat flux that is high enough to explain even the maximum observed melt rates.

https://doi.org/10.5194/egusphere-2023-1320
Preprint. Discussion started: 28 July 2023

Appendix E: Surface skin temperature

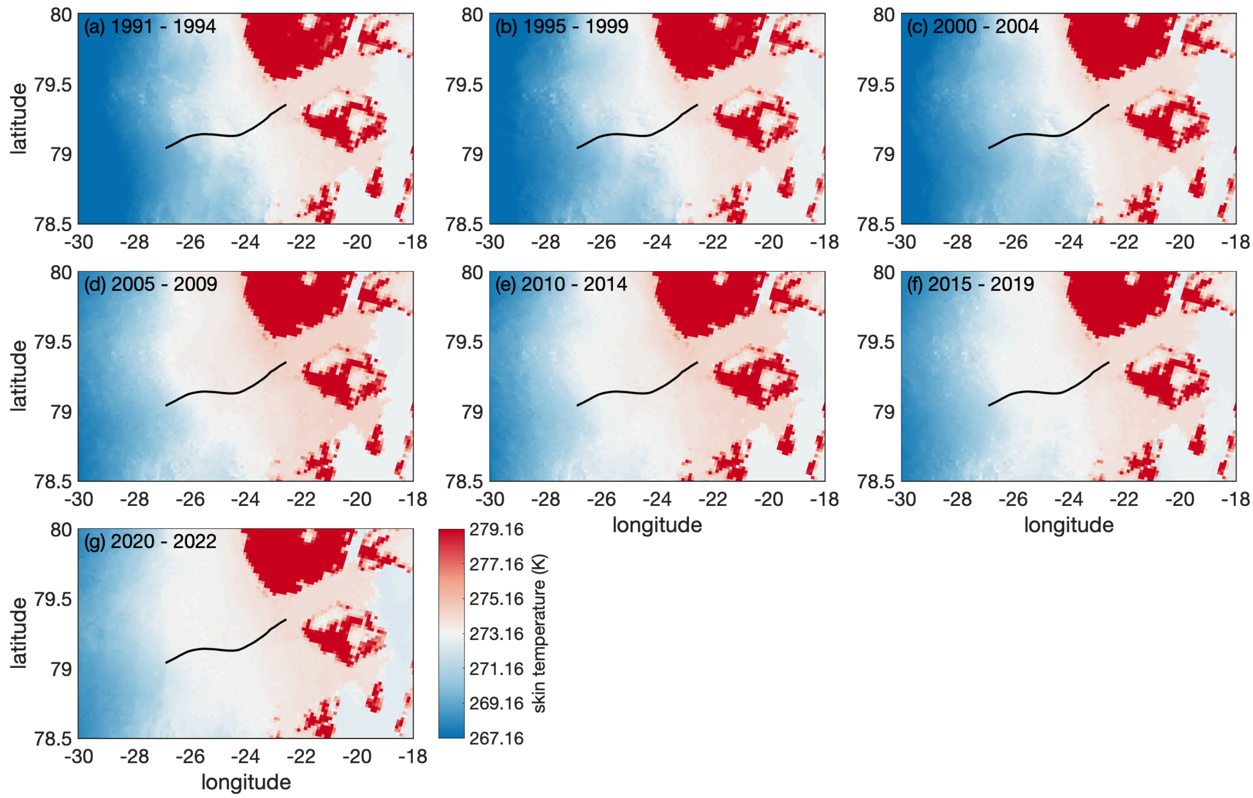

Figure E1. Skin temperature of 79NG between (a) 1991 – 1994, (b) 1995 – 1999, (c) 2000 – 2004, (d) 2005 – 2009, (e) 2010 – 2014, (f) 2015 – 2019 and (g) 2020 – 2022 from Copernicus Arctic Regional Reanalysis (Schyberg et al., 2020). The shown temperatures is the median skin temperature between 01 July and 31 August (at 15:00 UTC) of the given years.

Author contributions. OZ, DS, NN, and AH conducted the field expeditions, and AH and VH the airborne campaigns. AH has designed the study and planned field expeditions and airborne campaigns. OZ processed the (A)pRES data, and estimated and analyzed the resulting thinning and basal melt rates. ND processed the UWB 2018 data and discovered the central channel. VH processed the laser scanner data and the UWB 2021 data. NN processed all satellite data and determined the elevation changes and grounding line location. RT provided oceanographic expertise. OZ wrote the manuscript with contributions from all coauthors.

Competing interests. The contact author has declared that neither they nor their co-authors have any competing interests.

https://doi.org/10.5194/egusphere-2023-1320
Preprint. Discussion started: 28 July 2023

Acknowledgements. This study is part of the GROCE1 and GROCE2 projects funded by the German Federal Ministry of Research and Education under Grant No. 03F0778A and 03F0855A. NN has received funding from the European Union's Horizon 2020 research and innovation program under grant agreement No 689443 via project iCUPE (Integrative and Comprehensive Understanding on Polar Environments). The airborne data were acquired as part of AWI's RESURV79 (2018) and 79NG-EC (2021) campaigns with AWI's polar aircrafts (Wesche et al., 2016). We want to thank Tobias Binder and Martin Gehrmann, the aircraft crews, Will Wilson, Dean Emberly, Stewart Clark, Marc-André Verner, Luke Cirtwill, Ryan Schrader, the team of Villum Research Station, the Arctic Command and the team Station Nord in 2018 and 2021 for their support during the expeditions. TanDEM-X and TerraSAR-X data were made available through German Aerospace Center proposals GLAC7208 and HYD2059. The authors would like to thank Emerson E&P Software, Emerson Automation Solutions, for providing licenses in the scope of the Emerson Academic Program. We like to thank Steven Franke for his support in handling UWB data. We want to thank Jens Köhler and Graham Niven for their support in the field. We acknowledge the effort of Shfaqat Abbas Khan for servicing our ApRES during the lockdown in 2020 and retrieving our SD cards.

References

Bentley, M. J., Smith, J. A., Jamieson, S. S. R., Lindeman, M. R., Rea, B. R., Humbert, A., Lane, T. P., Darvill, C. M., Lloyd, J. M., Straneo, F., Helm, V., and Roberts, D. H.: Direct measurement of warm Atlantic Intermediate Water close to the grounding line of Nioghalvfjerdsfjorden (79° N) Glacier, northeast Greenland, The Cryosphere, 17, 1821–1837, https://doi.org/10.5194/tc-17-1821-2023, 2023.

Berthier, E., Cabot, V., Vincent, C., and Six, D.: Decadal Region-Wide and Glacier-Wide Mass Balances Derived from Multi-Temporal ASTER Satellite Digital Elevation Models. Validation over the Mont-Blanc Area, Frontiers in Earth Science, 4, 63, https://doi.org/10.3389/feart.2016.00063, 2016.

Brennan, P. V., Lok, L. B., Nicholls, K., and Corr, H.: Phase-sensitive FMCW radar system for high-precision Antarctic ice shelf profile monitoring, IET Radar, Sonar & Navigation, 8, 776–786, https://doi.org/10.1049/iet-rsn.2013.0053, 2014.

Choi, Y., Morlighem, M., Rignot, E., Mouginot, J., and Wood, M.: Modeling the response of Nioghalvfjerdsfjorden and Zachariae Isstrøm Glaciers, Greenland, to ocean forcing over the next century, Geophysical Research Letters, 44, 11–071, https://doi.org/10.1002/2017GL075174, 2017.

Ciracì, E., Rignot, E., Scheuchl, B., Tolpekin, V., Wollersheim, M., An, L., Milillo, P., Bueso-Bello, J.-L., Rizzoli, P., and Dini, L.: Melt rates in the kilometer-size grounding zone of Petermann Glacier, Greenland, before and during a retreat, Proceedings of the National Academy of Sciences, 120, e2220924 120, https://doi.org/10.1073/pnas.2220924120, 2023.

Corr, H. F., Jenkins, A., Nicholls, K. W., and Doake, C.: Precise measurement of changes in ice-shelf thickness by phase-sensitive radar to determine basal melt rates, Geophysical Research Letters, 29, 73–1–74–4, https://doi.org/10.1029/2001GL014618, 2002.

Cuffey, K. M. and Paterson, W. S. B.: The Physics of Glaciers - 4th ed., Elsevier, 2010.

Fahnestock, M. A., Joughin, I., Scambos, T. A., Kwok, R., Krabill, W. B., and Gogineni, S.: Ice-stream-related patterns of ice flow in the interior of northeast Greenland, Journal of Geophysical Research: Atmospheres, 106, 34 035–34 045, https://doi.org/10.1029/2001JD900194, 2001.

Fujita, S., Matsuoka, T., Ishida, T., Matsuoka, K., and Mae, S.: A summary of the complex dielectric permittivity of ice in the megahertz range and its applications for radar sounding of polar ice sheets, in: Physics of ice core records, pp. 185–212, Hokkaido University Press, 2000.

Fürst, J. J., Durand, G., Gillet-Chaulet, F., Tavard, L., Rankl, M., Braun, M., and Gagliardini, O.: The safety band of Antarctic ice shelves, Nature Climate Change, 6, 479, https://doi.org/10.1038/nclimate2912, 2016.

Hale, R., Miller, H., Gogineni, S., Yan, J.-B., Rodriguez-Morales, F., Leuschen, C., Paden, J., Li, J., Binder, T., Steinhage, D., et al.: Multichannel ultra-wideband radar sounder and imager, in: 2016 IEEE International Geoscience and Remote Sensing Symposium (IGARSS), pp. 2112–2115, IEEE, 2016.

Hellmer, H. H. and Olbers, D. J.: A two-dimensional model for the thermohaline circulation under an ice shelf, Antarctic Science, 1, 325–336, https://doi.org/10.1017/S0954102089000490, 1989.

Helm, V., Humbert, A., and Miller, H.: Elevation and elevation change of Greenland and Antarctica derived from CryoSat-2, The Cryosphere, 8, 1539–1559, https://doi.org/10.5194/tc-8-1539-2014, 2014.

Holland, D. M. and Jenkins, A.: Modeling thermodynamic ice–ocean interactions at the base of an ice shelf, Journal of Physical Oceanography, 29, 1787–1800, https://doi.org/10.1175/1520-0485(1999)029<1787:MTIOIA>2.0.CO;2, 1999.

Humbert, A., Helm, V., Neckel, N., Zeising, O., Rückamp, M., Khan, S. A., Loebel, E., Gross, D., Sondershaus, R., and Müller, R.: Precursor of disintegration of Greenland's largest floating ice tongue, The Cryosphere Discussions, 2022, 1–29, https://doi.org/10.5194/tc-2022-171, 2022a.

Humbert, A., Helm, V., Neckel, N., Zeising, O., Rückamp, M., Khan, S. A., Loebel, E., Gross, D., Sondershaus, R., and Müller, R.: Precursor of disintegration of Greenland's largest floating ice tongue, The Cryosphere Discussions [Preprint, Accpeted], 2022, 1–29, https://doi.org/10.5194/tc-2022-171, 2022b.

Jenkins, A.: Convection-driven melting near the grounding lines of ice shelves and tidewater glaciers, Journal of Physical Oceanography, 41, 2279–2294, https://doi.org/10.1175/JPO-D-11-03.1, 2011.

Jenkins, A. and Doake, C.: Ice-ocean interaction on Ronne Ice Shelf, Antarctica, Journal of Geophysical Research: Oceans, 96, 791–813, https://doi.org/10.1029/90JC01952, 1991.

Jenkins, A., Corr, H. F., Nicholls, K. W., Stewart, C. L., and Doake, C. S.: Interactions between ice and ocean observed with phase-sensitive radar near an Antarctic ice-shelf grounding line, Journal of Glaciology, 52, 325–346, https://doi.org/10.3189/172756506781828502, 2006.

Joughin, I., Smith, B. E., and Howat, I. M.: A complete map of Greenland ice velocity derived from satellite data collected over 20 years, Journal of Glaciology, 64, 1–11, https://doi.org/10.1017/jog.2017.73, 2018.

Khan, S. A., Kjær, K. H., Bevis, M., Bamber, J. L., Wahr, J., Kjeldsen, K. K., Bjørk, A. A., Korsgaard, N. J., Stearns, L. A., Van Den Broeke, M. R., et al.: Sustained mass loss of the northeast Greenland ice sheet triggered by regional warming, Nature Climate Change, 4, 292–299, https://doi.org/10.1038/nclimate2161, 2014.

Khan, S. A., Bamber, J. L., Rignot, E., Helm, V., Aschwanden, A., Holland, D. M., van den Broeke, M., King, M., Noël, B., Truffer, M., Humbert, A., Colgan, W., Vijay, S., and Kuipers Munneke, P.: Greenland Mass Trends From Airborne and Satellite Altimetry During 2011–2020, Journal of Geophysical Research: Earth Surface, 127, e2021JF006 505, https://doi.org/10.1029/2021JF006505, 2022a.

Khan, S. A., Choi, Y., Morlighem, M., Rignot, E., Helm, V., Humbert, A., Mouginot, J., Millan, R., Kjær, K. H., and Bjørk, A. A.: Extensive inland thinning and speed-up of Northeast Greenland Ice Stream, Nature, 611, 727–732, https://doi.org/10.1038/s41586-022-05301-z, 2022b.

King, M. D., Howat, I. M., Candela, S. G., Noh, M. J., Jeong, S., Noël, B. P. Y., van den Broeke, M. R., Wouters, B., and Negrete, A.: Dynamic ice loss from the Greenland Ice Sheet driven by sustained glacier retreat, Communications Earth & Environment, 1, 1, https://doi.org/10.1038/s43247-020-0001-2, 2020.

Kjeldsen, K. K., Korsgaard, N. J., Bjørk, A. A., Khan, S. A., Box, J. E., Funder, S., Larsen, N. K., Bamber, J. L., Colgan, W., Van Den Broeke, M., et al.: Spatial and temporal distribution of mass loss from the Greenland Ice Sheet since AD 1900, Nature, 528, 396–400, https://doi.org/10.1038/nature16183, 2015.

Krieger, L., Floricioiu, D., and Neckel, N.: Drainage basin delineation for outlet glaciers of Northeast Greenland based on Sentinel-1 ice velocities and TanDEM-X elevations, Remote Sensing of Environment, 237, 111 483, https://doi.org/10.1016/j.rse.2019.111483, 2020.

Le Brocq, A. M., Ross, N., Griggs, J. A., Bingham, R. G., Corr, H. F., Ferraccioli, F., Jenkins, A., Jordan, T. A., Payne, A. J., Rippin, D. M., et al.: Evidence from ice shelves for channelized meltwater flow beneath the Antarctic Ice Sheet, Nature Geoscience, 6, 945–948, https://doi.org/10.1038/ngeo1977, 2013.

Lindeman, M. R., Straneo, F., Wilson, N. J., Toole, J. M., Krishfield, R. A., Beaird, N. L., Kanzow, T., and Schaffer, J.: Ocean Circulation and Variability Beneath Nioghalvfjerdsbræ (79 North Glacier) Ice Tongue, Journal of Geophysical Research: Oceans, 125, e2020JC016 091, https://doi.org/10.1029/2020JC016091, 2020.

https://doi.org/10.5194/egusphere-2023-1320
Preprint. Discussion started: 28 July 2023

Loebel, E., Scheinert, M., Horwath, M., Humbert, A., Sohn, J., Heidler, K., Liebezeit, C., and Zhu, X. X.: Calving front monitoring at sub-seasonal resolution: a deep learning application to Greenland glaciers, The Cryosphere Discussions, 2023, 1–21, https://doi.org/10.5194/tc-2023-52, 2023.

Marsh, O. J., Fricker, H. A., Siegfried, M. R., Christianson, K., Nicholls, K. W., Corr, H. F., and Catania, G.: High basal melting forming a channel at the grounding line of Ross Ice Shelf, Antarctica, Geophysical Research Letters, 43, 250–255, https://doi.org/10.1002/2015GL066612, 2016.

Mayer, C., Reeh, N., Jung-Rothenhäusler, F., Huybrechts, P., and Oerter, H.: The subglacial cavity and implied dynamics under Nioghalvfjerdsfjorden Glacier, NE-Greenland, Geophysical Research Letters, 27, 2289–2292, https://doi.org/10.1029/2000GL011514, 2000.

Mayer, C., Schaffer, J., Hattermann, T., Floricioiu, D., Krieger, L., Dodd, P. A., Kanzow, T., Licciulli, C., and Schannwell, C.: Large ice loss variability at Nioghalvfjerdsfjorden Glacier, Northeast-Greenland, Nature Communications, 9, 2768, https://doi.org/10.1038/s41467-018-05180-x, 2018.

Morlighem, M., Williams, C. N., Rignot, E., An, L., Arndt, J. E., Bamber, J. L., Catania, G., Chauché, N., Dowdeswell, J. A., Dorschel, B., Fenty, I., Hogan, K., Howat, I., Hubbard, A., Jakobsson, M., Jordan, T. M., Kjeldsen, K. K., Millan, R., Mayer, L., Mouginot, J., Noël, B. P. Y., O'Cofaigh, C., Palmer, S., Rysgaard, S., Seroussi, H., Siegert, M. J., Slabon, P., Straneo, F., van den Broeke, M. R., Weinrebe, W., Wood, M., and Zinglersen, K. B.: BedMachine v3: Complete bed topography and ocean bathymetry mapping of Greenland from multibeam echo sounding combined with mass conservation, Geophysical Research Letters, 44, 11 051–11 061, https://doi.org/10.1002/2017GL074954, 2017.

Morlighem, M., Williams, C., Rignot, E., An, L., Arndt, J. E., Bamber, J., Catania, G., Chauché, N., Dowdeswell, J. A., Dorschel, B., Fenty, I., Hogan, K., Howat, I., Hubbard, A., Jakobsson, M., Jordan, T. M., Kjeldsen, K. K., Millan, R., Mayer, L., Mouginot, J., Noël, B., O'Cofaigh, C., Palmer, S. J., Rysgaard, S., Seroussi, H., Siegert, M. J., Slabon, P., Straneo, F., van den Broeke, M. R., Weinrebe, W., Wood, M., and Zinglersen, K.: IceBridge BedMachine Greenland, Version 5, https://doi.org/10.5067/GMEVBWFLWA7X, 2022.

Motyka, R. J., Truffer, M., Fahnestock, M., Mortensen, J., Rysgaard, S., and Howat, I.: Submarine melting of the 1985 Jakobshavn Isbræ floating tongue and the triggering of the current retreat, Journal of Geophysical Research: Earth Surface, 116, https://doi.org/10.1029/2009JF001632, 2011.

Mouginot, J., Rignot, E., Scheuchl, B., Fenty, I., Khazendar, A., Morlighem, M., Buzzi, A., and Paden, J.: Fast retreat of Zachariæ Isstrøm, northeast Greenland, Science, 350, 1357–1361, https://doi.org/10.1126/science.aac7111, 2015.

Münchow, A., Padman, L., and Fricker, H. A.: Interannual changes of the floating ice shelf of Petermann Gletscher, North Greenland, from 2000 to 2012, Journal of Glaciology, 60, 489–499, https://doi.org/10.3189/2014JoG13J135, 2014.

Münchow, A., Schaffer, J., and Kanzow, T.: Ocean Circulation Connecting Fram Strait to Glaciers off Northeast Greenland: Mean Flows, Topographic Rossby Waves, and Their Forcing, Journal of Physical Oceanography, 50, 509 – 530, https://doi.org/doi.org/10.1175/JPO-D-19-0085.1, 2020.

Neckel, N., Braun, A., Kropáček, J., and Hochschild, V.: Recent mass balance of the Purogangri Ice Cap, central Tibetan Plateau, by means of differential X-band SAR interferometry, The Cryosphere, 7, 1623–1633, https://doi.org/10.5194/tc-7-1623-2013, 2013.

Nicholls, K. W., Corr, H. F., Stewart, C. L., Lok, L. B., Brennan, P. V., and Vaughan, D. G.: A ground-based radar for measuring vertical strain rates and time-varying basal melt rates in ice sheets and shelves, Journal of Glaciology, 61, 1079–1087, https://doi.org/10.3189/2015JoG15J073, 2015.

Nuth, C. and Kääb, A.: Co-registration and bias corrections of satellite elevation data sets for quantifying glacier thickness change, The Cryosphere, 5, 271–290, https://doi.org/10.5194/tc-5-271-2011, 2011.

Rathmann, N., Hvidberg, C., Solgaard, A., Grinsted, A., Gudmundsson, G. H., Langen, P. L., Nielsen, K., and Kusk, A.: Highly temporally resolved response to seasonal surface melt of the Zachariae and 79N outlet glaciers in northeast Greenland, Geophysical Research Letters, 44, 9805–9814, https://doi.org/10.1002/2017GL074368, 2017.

Reinert, M., Lorenz, M., Klingbeil, K., Büchmann, B., and Burchard, H.: High-resolution simulations of the plume dynamics in an idealized 79°N Glacier cavity using adaptive vertical coordinates [Preprint], ESS Open Archive, https://doi.org/10.22541/essoar.167979227.75015410/v1, 2023.

Ritz, C.: Time dependent boundary conditions for calculation of temperature fields in ice sheets, in: The Physical Basis of Ice Sheet Modelling, edited by Waddington, E. D. and Walder, J. S., IAHS Publication No. 170, pp. 207–216, IAHS Press, Wallingford, UK, 1987.

Schaffer, J., Kanzow, T., von Appen, W.-J., von Albedyll, L., Arndt, J. E., and Roberts, D. H.: Bathymetry constrains ocean heat supply to Greenland's largest glacier tongue, Nature Geoscience, 13, 227–231, https://doi.org/10.1038/s41561-019-0529-x, 2020.

Schyberg, H., Yang, X., Køltzow, M. A. O., Amstrup, B., Bakketun, A., Bazile, E., Bojarova, J., Box, J. E., Dahlgren, P., Hagelin, S., Homleid, M., Horányi, A., Høyer, J., Johansson, A., Killie, M. A., Körnich, H., Le Moigne, P., Lindskog, M., Manninen, T., Nielsen Englyst, P., Nielsen, K. P., Olsson, E., Palmason, B., Peralta Aros, C., Randriamampianina, R., Samuelsson, P., Stappers, R., Støylen, E., Thorsteinsson, S., and Valkonen, T. amd Wang, Z. Q.: Arctic regional reanalysis on single levels from 1991 to present, Copernicus Climate Change Service (C3S) Climate Data Store (CDS) [data set], https://doi.org/10.24381/cds.713858f6, 2020.

Shepherd, A., Ivins, E., Rignot, E., Smith, B., van den Broeke, M., Velicogna, I., Whitehouse, P., Briggs, K., Joughin, I., Krinner, G., Nowicki, S., Payne, T., Scambos, T., Schlegel, N., A, G., Agosta, C., Ahlstrøm, A., Babonis, G., Barletta, V. R., Bjørk, A. A., Blazquez, A., Bonin, J., Colgan, W., Csatho, B., Cullather, R., Engdahl, M. E., Felikson, D., Fettweis, X., Forsberg, R., Hogg, A. E., Gallee, H., Gardner, A., Gilbert, L., Gourmelen, N., Groh, A., Gunter, B., Hanna, E., Harig, C., Helm, V., Horvath, A., Horwath, M., Khan, S., Kjeldsen, K. K., Konrad, H., Langen, P. L., Lecavalier, B., Loomis, B., Luthcke, S., McMillan, M., Melini, D., Mernild, S., Mohajerani, Y., Moore, P., Mottram, R., Mouginot, J., Moyano, G., Muir, A., Nagler, T., Nield, G., Nilsson, J., Noël, B., Otosaka, I., Pattle, M. E., Peltier, W. R., Pie, N., Rietbroek, R., Rott, H., Sandberg Sørensen, L., Sasgen, I., Save, H., Scheuchl, B., Schrama, E., Schröder, L., Seo, K.-W., Simonsen, S. B., Slater, T., Spada, G., Sutterley, T., Talpe, M., Tarasov, L., van de Berg, W. J., van der Wal, W., van Wessem, M., Vishwakarma, B. D., Wiese, D., Wilton, D., Wagner, T., Wouters, B., Wuite, J., and Team, T. I.: Mass balance of the Greenland Ice Sheet from 1992 to 2018, Nature, 579, 233–239, https://doi.org/10.1038/s41586-019-1855-2, 2020.

Shroyer, E. L., Padman, L., Samelson, R., Münchow, A., and Stearns, L. A.: Seasonal control of Petermann Gletscher ice-shelf melt by the ocean's response to sea-ice cover in Nares Strait, Journal of Glaciology, 63, 324–330, https://doi.org/10.1017/jog.2016.140, 2017.

Slater, D. A., Felikson, D., Straneo, F., Goelzer, H., Little, C. M., Morlighem, M., Fettweis, X., and Nowicki, S.: Twenty-first century ocean forcing of the Greenland ice sheet for modelling of sea level contribution, The Cryosphere, 14, 985–1008, https://doi.org/10.5194/tc-14-985-2020, 2020.

Stewart, C. L.: Ice-ocean interactions beneath the north-western Ross Ice Shelf, Antarctica, Ph.D. thesis, University of Cambridge, https://doi.org/10.17863/CAM.21483, 2018.

Stewart, C. L., Christoffersen, P., Nicholls, K. W., Williams, M. J., and Dowdeswell, J. A.: Basal melting of Ross Ice Shelf from solar heat absorption in an ice-front polynya, Nature Geoscience, 12, 435–440, https://doi.org/10.1038/s41561-019-0356-0, 2019.

Straneo, F., Sutherland, D. A., Holland, D., Gladish, C., Hamilton, G. S., Johnson, H. L., Rignot, E., Xu, Y., and Koppes, M.: Characteristics of ocean waters reaching Greenland's glaciers, Annals of Glaciology, 53, 202–210, https://doi.org/10.3189/2012AoG60A059, 2012.

Straneo, F., Hamilton, G. S., Stearns, L. A., and Sutherland, D. A.: Connecting the Greenland Ice Sheet and the Ocean: A Case Study of Helheim Glacier and Sermilik Fjord, Oceanography, 29, 34–45, https://doi.org/10.5670/oceanog.2016.97, 2016.

https://doi.org/10.5194/egusphere-2023-1320
Preprint. Discussion started: 28 July 2023

The MathWorks Inc.: MATLAB version: 9.13.0 (R2022b), https://www.mathworks.com, 2022.

Thomsen, H. H., Reeh, N., Olesen, O. B., Bøggilde, C. E., Starzer, W., Weidick, A., and Higgins, A.: The Nioghalvfjerdsfjorden glacier project, North-East Greenland: a study of ice sheet response to climatic change, Review of Greenland activities, pp. 95–103, https://doi.org/10.34194/ggub.v176.5073, 1997.

Timmermann, R., Wang, Q., and Hellmer, H.: Ice-shelf basal melting in a global finite-element sea-ice/ice-shelf/ocean model, Annals of Glaciology, 53, 303–314, https://doi.org/10.3189/2012AoG60A156, 2012.

Vaňková, I., Cook, S., Winberry, J. P., Nicholls, K. W., and Galton-Fenzi, B. K.: Deriving Melt Rates at a Complex Ice Shelf Base Using In Situ Radar: Application to Totten Ice Shelf, Geophysical Research Letters, 48, e2021GL092 692, https://doi.org/10.1029/2021GL092692, 2021.

Vijay, S., Khan, S. A., Kusk, A., Solgaard, A. M., Moon, T., and Bjørk, A. A.: Resolving Seasonal Ice Velocity of 45 Greenlandic Glaciers With Very High Temporal Details, Geophysical Research Letters, 46, 1485–1495, https://doi.org/10.1029/2018GL081503, 2019.

von Albedyll, L., Schaffer, J., and Kanzow, T.: Ocean Variability at Greenland's Largest Glacier Tongue Linked to Continental Shelf Circulation, Journal of Geophysical Research: Oceans, 126, e2020JC017 080, https://doi.org/10.1029/2020JC017080, 2021.

Washam, P., Nicholls, K. W., Münchow, A., and Padman, L.: Summer surface melt thins Petermann Gletscher Ice Shelf by enhancing channelized basal melt, Journal of Glaciology, 65, 662–674, https://doi.org/10.1017/jog.2019.43, 2019.

Wesche, C., Steinhage, D., and Nixdorf, U.: Polar aircraft Polar5 and Polar6 operated by the Alfred Wegener Institute, Journal of large-scale research facilities, 2, 1–7, https://doi.org/10.17815/jlsrf-2-153, 2016.

Wessel, B., Bertram, A., Gruber, A., Bemm, S., and Dech, S.: A new high-resolution elevation model of Greenland derived from TanDEM-X, in: XXIII ISPRS Congress, vol. III-7, pp. 9–16, https://doi.org/10.5194/isprs-annals-III-7-9-2016, 2016.

Wilson, N. and Straneo, F.: Water exchange between the continental shelf and the cavity beneath Nioghalvfjerdsbræ (79 North Glacier), Geophysical Research Letters, 42, 7648–7654, https://doi.org/10.1002/2015GL064944, 2015.

Wilson, N., Straneo, F., and Heimbach, P.: Satellite-derived submarine melt rates and mass balance (2011-2015) for Greenland's largest remaining ice tongues, The Cryosphere, 11, 2773–2782, https://doi.org/10.5194/tc-11-2773-2017, 2017.

Zeising, O., Neckel, N., Steinhage, D., Scheinert, M., and Humbert, A.: Stake surface ablation/accumulation measurements at 79°N Glacier between 2017 and 2018 [data set], https://doi.org/10.1594/PANGAEA.922131, 2020.